Optically detected magnetic resonance with an open source platform

Hossein Babashah,[1] Hoda Shirzad,[1] Elena Losero,[1] Valentin Goblot,[1] Christophe Galland,[1] and Mayeul Chipaux[1]
Institute of Physics, École Polytechnique Fédérale de Lausanne (EPFL), Lausanne CH-1015, Switzerland
H.S and H.B. contributed equally to this work.

(*Electronic mail: mayeul.chipaux@epfl.ch)

(Dated: 3 May 2022)

Localized electronic spins in solid-state environments form versatile and robust platforms for quantum sensing, metrology and quantum information processing. With optically detected magnetic resonance (ODMR), it is possible to prepare and readout highly coherent spin systems, up to room temperature, with orders of magnitude enhanced sensitivities and spatial resolutions compared to induction-based techniques, allowing single spin manipulations. While ODMR was first observed in organic molecules, many other systems are nowadays intensively being searched for, discovered and studied. Among them is the nitrogen-vacany (NV) center in diamond. Beyond ODMR it is notably already widely and successfully used both as a high-resolution high-sensitivity quantum sensors for external fields and as a qubit. Others are rare earth ions used as quantum memories and many other color centers trapped in bulk or 2-dimensional materials. In order to allow the broadest possible community of researchers and engineers to investigate and develop novel ODMR-based materials and applications, we overview here the setting up of ODMR experiments using commercially available hardware. We also present in detail a dedicated collaborative open-source interface named Qudi and describe the original features we have added to speed-up data acquisition, relax instrumental requirements and widen its applicability to individual and ensemble ODMR systems. Associating hardware and software discussions, this article aims to steepen the learning curve of newcomers in ODMR from a variety of scientific backgrounds, to optimize the experimental development time, preempt the common measurement pitfalls, and to provide an efficient, portable and collaborative interface to explore innovative experiments.

CONTENTS

INTRODUCTION

Spin is a quantum property of elementary particles which confers them an intrinsic magnetic moment that can be associated with a circulating charge flow in their wave function[1]. In atoms and ions, while the nuclear spins remain essentially shielded, the unpaired electrons result in magnetic moments

that are three order of magnitude stronger – of the order of the Bohr magneton. It makes electron spins the main contributors to most materials' magnetic properties. In the modern context of the second quantum revolution[2], electron spins, such as in quantum dots[3,4], color centers in diamond[5] or silicon carbide[6], or rare earth ions[7] have been either studied as individual quantum systems or as ensembles. While electron spins naturally interact with various external and internal fields, they can also be isolated from unwanted perturbations by experimental design or choice of system[8], making them either great quantum sensors[9] or highly coherent quantum bits (or qubits) for quantum information processing[10,11].

Standard inductive radio- and microwave techniques for spin resonance measurements suffer from poor sensitivity and low spatial resolution. Indeed, under achievable magnetic fields electronic spin transition energies typically lie in the microwave (MW) domain, with associated Boltzmann temperatures of few tens of millikelvin, so that they are very weakly polarized in ambient conditions. Additionally, sensing MW fields at the single photon level remains a tremendous challenge[12], while this electromagnetic domains is associated with wavelengths from millimeters to centimeters, by far larger than the few tens of nanometers required for directly probing spin-spin interactions[13]. Even using magnetic field gradients Magnetic Resonance Imaging (MRI) cannot achieve spatial resolution below tens of micrometers[14]. All these limitations affect both the spatial resolutions in quantum sensing and the scaling of entangled qubits' networks for useful quantum computing.

Optical Detection of Magnetic Resonance (ODRM)[15] offers a powerful solution to these problems. It is applicable to a range of material systems (see Table I) whose joint optical and magnetic properties render their electron-spin magnetic transition detectable in the optical domain. The following ingredients are characteristics of ODMR systems: Firstly, the electronic spin can be polarized by optical pumping to a much higher degree than under thermal equilibrium. Associated with naturally low spin-lattice coupling[16], certain electronic spins can maintain long polarization and coherence times even at elevated temperature[17]. Together those properties can, totally relax the need for cryogenic conditions. Secondly, the strength of optical signal (typically absorption or fluorescence or phosphorescence) must depend on the electronic spin state or its projection along a quantization axis. Since optical fields can routinely be detected at the shot-noise limit, the sensitivity of magnetic resonance spectroscopy and the fidelity of spin state readout can be significantly increased while spin initialization and readout can be achieved with a much higher spatial resolution set by the optical wavelength. Finally, these advantages can be translated to nuclear spin spectroscopy through the use of hyperfine coupling[18]. Together, these features are placing ODMR at the core of many emerging spin-based quantum technologies.

Despite the growing number of researchers and engineers active in this area and the availability of advanced optical and microwave (MW) equipment, building and operating an ODMR setup for a specific purpose usually demands substantial hardware and software developments. Moreover, beyond the apparent simplicity of ODMR measurements, a certain amount of tacit knowledge is needed to avoid some pitfalls that can spoil measurement accuracy and reproducibility. The main goals of this article are (i) to describe the typical ODMR setups, from its conception and construction to the optimization of specific measurements and (ii) to present the recently developed features that we added to the ODMR dedicated open source platform Qudi[19] for speeding-up acquisitions, relaxing instrumental requirements, widen its applications and lowering newcomers' entry barrier.

In Sec. I, we first recall ODMR main principles and measurement techniques and overview of the most studied systems with their applications. We then present the hardware configuration needed for ODMR experiments in Sec. II. Aspects related to optical setup, generation of MWs signals and pulses and of bias magnetic fields are discussed. We show how some ODMR experiments (in continuous wave and pulsed modes) can be visualized directly with an oscilloscope, and determine when the use of a computer interface is useful or required. In Sec. III, we describe how these instruments are connected together and present the most common strategies for synchronizing ODMR experiments. Both the computer and oscilloscope interfaces are covered. Section IV is dedicated to the open source platform Qudi, first release in 2017[19], for operating ODMR experiments. With a focus on the features we added to Qudi, the section is written as a user guide for getting started and it addresses the main issues related to interfacing with specific hardware. Finally, in Sec. V we give a few practical advice to perform reliable and contrasted measurements, in particular accounting for technical noise and instrument imperfections. We take a specific focus on NV center ensembles as an illustrative scenario.

We believe that the software development and technical guide presented here will help newcomers achieve faster and better results for their desired application and provide experts an efficient, portable, and collaborative platform to explore innovative experiments.

I. OPTICALLY DETECTED MAGNETIC RESONANCE

A. Main principles

ODMR relies on two main features: (i) initialization (*i.e.* polarization) of the spin state under optical excitation (spin pumping) and (ii) spin-state-dependent optical properties, such as fluorescence, phosphorescence, absorption, or, as more recently demonstrated, photocurrent[20], used for spin state readout. While feature (i) boosts the spin resonance signal, feature (ii) allows to advantageously trade low energy MW photons for much higher energy optical ones in the spin state measurement. These properties may arise from spin-orbit coupling (see Fig. 1), a relativistic effect that allows for Inter-System Crossing (ISC), *e.g.* transitions between singlet $S = 0$ and triplet $S = 1$ state manifolds[21,22]. The probability of ISC may depend on the initial spin state, which in turn may result in spin-dependent optical properties and spin-dependent

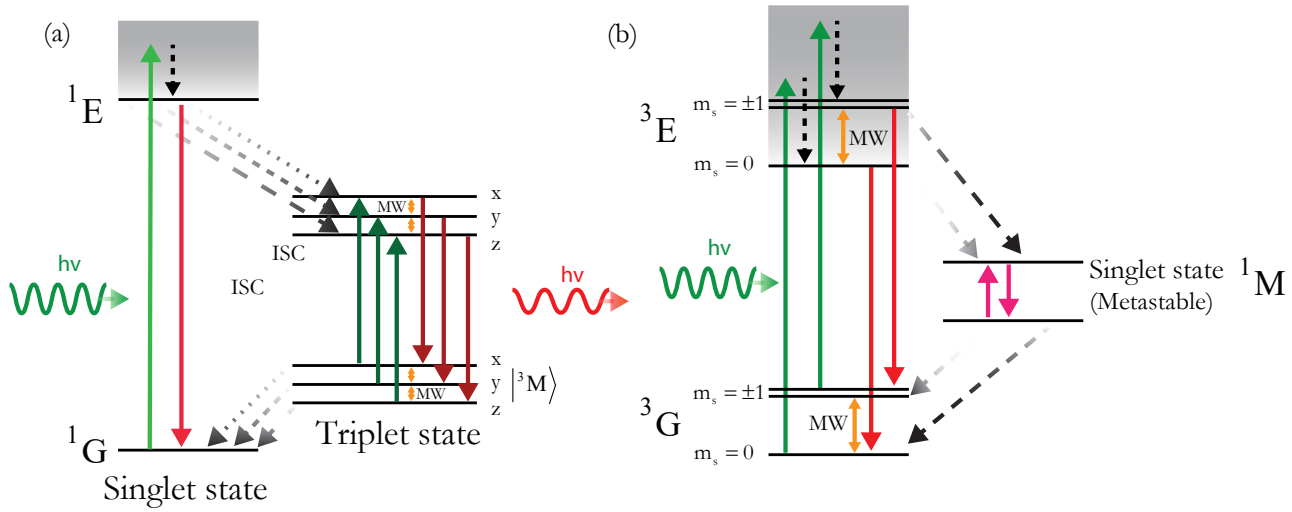

FIG. 1. InterSystem Crossing (ISC) based ODMR dynamics when the ground state is singlet (a) or triplet (b).

relaxation pathways. In other systems (see Sec. I C), ODMR can be achieved under resonant optical pumping such as using lambda shaped configurations.

B. Interactions with external quantities

Spin triplet state undergo specific interactions. At first, if the systems is not isotropic, a quantization axis emerges. Noting m_S the spin quantum number (*i.e.* the spin projection along that axis), the dipolar spin-spin interaction lifts the degeneracy between the states $|m_S = 0\rangle$ and $|m_S = \pm 1\rangle$, by an amount called Zero-field splitting (ZFS), often denoted with D. Further degeneracy is lifted between $|m_S = -1\rangle$ and $|m_S = +1\rangle$ by a parameter E when the symmetry is less than axial. The eigenstates, potentially made of superpositions of pure spin states, are then often denoted x, y and z. D and E depend on geometrical aspects and therefore on pressure and temperature. In addition, Stark and Zeeman effects further separate the $|m_S = -1\rangle$ and $|m_S = +1\rangle$ state which makes ODMR systems naturally sensitive to magnetic and electric fields. Finally, further interactions may occur with other electron or nuclear spins, resulting in more level splittings, spin dephasing and diffusion, etc.

C. Main ODMR systems and their applications

We can distinguish two main configurations linked to the multiplicity of the ground state (see Fig. 1). The ground state of organic molecules are typically spin singlets, where all electrons are paired in covalent bonds or lone pairs[23]. Photoexcitation followed by ISC may promote the molecule into a spin triplet state and enable ODMR as in Fig. 1 (a). Since 1967[24–26], such process has been exploited to enhance the detection limit of magnetic resonance[23] with a particular application in photosynthesis research[27,28]. ODMR from a single molecule was reported for the first time in 1993 independently by Wrachtrup *et. al.*[29] and Köhler, *et. al.*[30]. Both experiments relied on the photoexcited metastable triplet state of a pentacene molecule trapped in a p-terphenyl host crystal. Pentacene's spin-dependent optical properties have also been used inside MW resonators[31], such as for demonstrating the first room temperature maser[32] or conversely for cooling a microwave mode[33].

The negatively charged Nitrogen-Vacancy center (NV^-) in diamond - hereafter called NV center - belongs to the second configuration depicted in Fig. 1 (b). Its ground $^3A_2$ and main excited ^{3}E optical states are already spin triplets, while ISC offers a spin selective relaxation path through a metastable singlet state. The first single NV center ODMR signal was reported by Gruber *et. al.* in 1997[34]. For the following reasons, NV centers then became the most studied ODMR system. Firstly, they are highly photostable over a wide range of temperatures[35], pressures[35], and biological conditions . This feature also makes NV-doped nanodiamonds particularly relevant in biological environment[36] when used as biomarker[37–39] or quantum sensors[40,41]. Besides, NV centers can exhibit long spin relaxation and coherence times[17] thanks to the low density of nuclear spins in diamond and the decoupling of spin states from lattice phonons[16]. It makes them versatile quantum sensors[42] for detection and imaging of magnetic and electric fields, temperature, strain, currents and associated noises[9,43,44], as well as for microwave field imaging[45] or spectroscopy[46,47]. In addition, NV center ODMR properties can be extended to polarize[48–50] and/or detect[51–54] other electron or nuclear spins in their vicinity. In these cases the sensitivity can go down to a single nuclear spin, orders of magnitude better than conventional electron paramagnetic resonance (EPR) and nuclear magnetic resonance (NMR) methods. Finally, thanks to their excellent coherence properties and couplings to even longer lived nuclear spins[55], NV centers are also promising qubits for

quantum information processing[11] and fundamental studies of quantum mechanics[56].

Other diamond defects from the group IV-vacancy category[57] have recently revealed their ODMR signals. This is for instance the case of the negatively charged silicon-vacancy center (SiV^-)[58] and of its neutral form (SiV^0)[59] as well as of the Germanium-Vacancy (GeV)[60] and of the Tin-Vacancy (SnV)[61] centers. In those cases, the ODMR scheme requires low temperature operations so to allow resonant optical addressing differing from the one presented Fig. 1.

In other crystals, single defect ODMR signals have recently been reported in silicon carbide[6,62,63] or hexagonal boron nitride[64,65]. Notably, the so called V1 center in silicon carbide[62] involves a spin quartet $S = \frac{3}{2}$ ground state.

Rare earth ions is crystal lattices are also intensely studied for long lasting and broadband optical quantum memories[66,67]. One can cite Ce^{3+} in YAG[68] or Yb^{3+}[69] and Eu^{3+}[70] in Y_2SiO_5. Semiconductor quantum dots have also been used in ODMR experiments[71,72].

The optical wavelengths and microwave frequencies associated to those systems are listed in Table I.

D. Main ODMR techniques

1. *Continuous wave mode*

ODMR can be performed under continuous wave (CW) optical and MW excitation. A CW-ODMR spectrum is obtained by recording the optical emission or absorption as function of the MW frequency that is being swept. When spin resonances are reached, dips or peaks appear in the recorded optical intensity (see Fig. 2). Typically, this allows to localized the ODMR resonances frequencies of the system to either measure the physical parameters that govern it or determine gyromagnetic ratio of the system itself (EPR spectroscopy). Several parameters affect the precision of the spectrum obtained by CW-ODMR through the change in signal-to-noise ratio and spin resonance linewidth. These parameters include MW power (via power broadening[76] and sample heating), laser power (via change in excitation rate, governing spin polarization, optical emission and photo-ionization rates), MW sweeping method and pace, etc. Optimization of CW-ODMR signal acquisition is discussed in Sec. V B.

2. *Pulse sequences*

Pulsed ODMR has the first advantage of mitigating power broadening by letting the system evolve freely after optical and MW excitations. It also allows to tune the system for being specifically sensitive to certain quantities and insensitive to unwanted perturbations, taking advantage of decades of development in the field of magnetic resonance spectroscopy[77]. Good practices for optimizing a pulsed ODMR signal are discussed in Sec. V C. Below, we first introduce most common pulse sequences (in the case of a spin triplet).

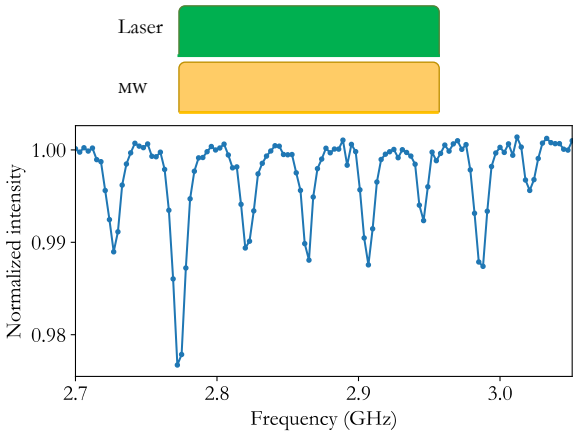

FIG. 2. Example of a continuous-wave ODMR spectrum from an NV-center ensemble under d.c. magnetic field, displaying eight resonances (hyperfine splitting not resolved) with contrasts on the order of 1%.

Common to most sequences, a first laser pulse initializes the system (*e.g.* in state $|m_S = 0\rangle$). After a period of spin manipulation with MW pulses and/or free evolution, a second laser pulse interrogates the spin state projection along the $(|m_S = 0\rangle, |m_S = +1\rangle)$ basis through the optical emission or absorption intensity. It also re-initializes the system for the subsequent measurement. In the Bloch sphere representation, a MW π pulse performs a π rotation along a certain axis, for instance, it can swap the $|m_S = 0\rangle$ and $|m_S = +1\rangle$ (or $|m_S = -1\rangle$). A $\pi/2$ pulse only performs a quarter turn, placing an initial $|m_S = 0\rangle$ state into an equal superposition $\frac{1}{\sqrt{2}}\left(|m_S = 0\rangle + e^{i\phi}|m_S = +1\rangle\right)$ (or $|-1\rangle$).

Relaxometry – T_1 measurement — This sequence, reported in Fig. 3(a), requires no MW fields. The two initialization and readout optical pulses are separated by a varying dark time τ. It allows probing the relaxation dynamics from an initialized pure state to a thermal equilibrium. Interesting for applications, the relaxation time, or T_1, can sense the magnetic noise of the local environment[78,79] such as the one created by free radicals species in living cells[40] or by chemical reactions[80].

Rabi sequence – π pulse calibration — In this sequence, reported in Fig. 3(b), the delay between the optical pulses is fixed and a MW pulse is applied for a varying duration τ (alternatively, its power can be varied). The measured optical signal as a function of τ shows Rabi oscillations. From this measurement the duration of π and $\frac{\pi}{2}$ pulses can be inferred as half and quarter periods of the oscillations, respectively.

Ramsey sequence – T_2^* measurement — This sequence, reported in Fig. 3(c), consists in a pump-probe experiment where two $\pi/2$ pulses are inserted. The first $\pi/2$, immediately after the initialization laser pulse, induces spin precession. After the free evolution time τ the precession is halted by a second $\pi/2$ pulse before the read-out laser pulse is applied. The optical signal as function of τ presents oscillations at the difference-frequency between the applied MW field and

System (host)	**Optical pumping** Off resonance pumping (On resonance (ZPL))	**Microwave** Zero field splitting D (E) Gyromagnetic ratio $\{\gamma\}$	**Comments / Applications**
Organic molecules	Various	$D = 500$ to $1500\,\mathrm{MHz}$ ($E = 0$ to $500\,\mathrm{MHz}$)	Sensitive EPR spectroscopy[23] Photosynthesis[73]
Pentacene (p-terphenyl crystal)	Green - yellow, *e.g.* 585 nm	$D = 1395\,\mathrm{MHz}$ ($E = 53\,\mathrm{MHz}$)	First a single molecule ODMR signal[29,30] First room temperature maser[31,32]
NV$^-$ center (Diamond)	Green *e.g.* 515 or 532 nm (637 nm = 1.945 eV)	$D = 2.87\,\mathrm{GHz}$ $\{\gamma = 28\,\mathrm{GHz\,T^{-1}}\}$	Quantum sensing Quantum computation
Group IV-Vacancy centers (Diamond)			On resonance, Cryogenic temperature.[74] Quantum networks[75]
SiV$^-$	(737 nm)	$D = 50\,\mathrm{GHz}$	[58]
SiV^0	(946 nm)	$D = 944\,\mathrm{GHz}$	[59]
GeV	(612 nm)	$D = 170\,\mathrm{GHz}$	[60]
SnV	(260 nm)		[61]
V1 center	(861 nm)	$D = 2\,\mathrm{MHz}$	Spin quartet[62]
PL8 center (4H-Silicon carbide)	920 nm (1007 to 1024 nm)	$D = 1.39\,\mathrm{GHz}$ $E = 4\,\mathrm{MHz}$	Room temperature[63] [6]
Unknown defects (Boron Nitride)	532 nm	$D = 0.1$ to $2.4\,\mathrm{GHz}$	[64]
Rare earth ions			Quantum memories[66,67]
Ce^{3+} (YAG)	(460 and 486 nm)	$< 22.2\,\mathrm{GHz}$	[68]
Yb^{3+} (Y_2SiO_5)	(980 nm)	$< 2.62\,\mathrm{GHz}$	[69]
Eu^{3+} (Y_2SiO_5)	(580 nm)	34.5 and 46.2 MHz	[70]
Quantum dots			
(In,Al)As/(AlAs)	404 nm		[71]
CdSe/(Cd,Mn)S	405 nm	60 GHz	[72]

TABLE I. ODMR systems.

the spin transition being probed. Therefore, this sequence can be used for DC sensing and offers better sensitivity compared to the CW-ODMR approach[76] by eluding the detrimental effect of power broadening. Ramsey fringes are damped with a time constant reflecting the spin dephasing time or heterogeneous decoherence time called T_2^*.

Hahn echo sequence – T_2 measurement — This sequence, reported in Fig. 3(d), uses a π pulse in the middle of the Ramsey sequence. This approach mitigates the effect of slowly fluctuating fields (such as from the nuclear spin bath) by canceling in the second half of the evolution the accumulated phase difference from the first half and restoring the original coherence. The characteristic decay time measured with this protocol is usually called T_2, and can typically be one or two orders of magnitude longer than T_2^*. More and more complex and faster dynamical decoupling sequences can be employed to extend T_2; yet, it remains bounded by relaxation time through $T_2 < 2 \cdot T_1$. Such echo sequence is particularly suitable of a.c. field sensing as it can filter a narrow frequency window[9].

Many efforts have been devoted to develop and optimize pulse sequences for increasing sensitivities to specific quantities and frequencies while canceling other noises. A comprehensive review dedicated to NV centers can be found in[42].

II. HARDWARE FOR CONTINUOUS AND PULSED ODMR

In this section we review the instrumental requirements for ODMR measurements in terms of optical setup, MW generation and biased magnetic field. Both CW and pulsed ODMR measurements are discussed.

A. Photoluminescence microscopy

As mentioned in Sec. I, ODMR relies on monitoring an optical signal such as photoluminescence (PL). It is obtained by directing a pumping beam (a laser or LED) onto the system of interest and routing the luminescence signal onto a photodectector (such as an amplified photodiode, a single photon counting module or a camera).

The simple optical setup reported in Fig. 4 is analogous to an epifluorescence microscope. An excitation laser beam is reflected on a dichroic mirror and focused on the sample via a microscope objective or a simple lens. The sample's luminescence is collected by the same lens and sent to a photodetector. Alternatively, the sample can be pumped from another side or by total internal reflection[81–83], to relax the need of a dichroic mirror or optimize pump power utilization and spa-

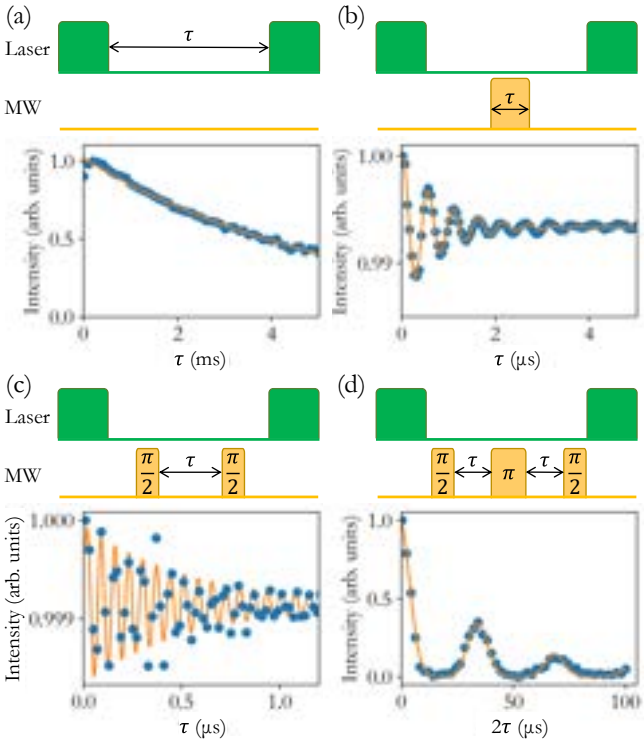

FIG. 3. Most common pulse sequences for ODMR: a) Relaxometry b) Rabi sequence c) Ramsey sequence d) Hahn echo sequence. In each panel, laser and MW pulses are represented schematically in the top part. In the bottom part, NV centers' experimental data obtained in our set-up from are shown.

tial homogeneity of excitation. An inverted configuration of the microscope (*e.g.* where the objective is below the sample) can be chosen when using liquid immersion objectives, especially for biological applications[84].

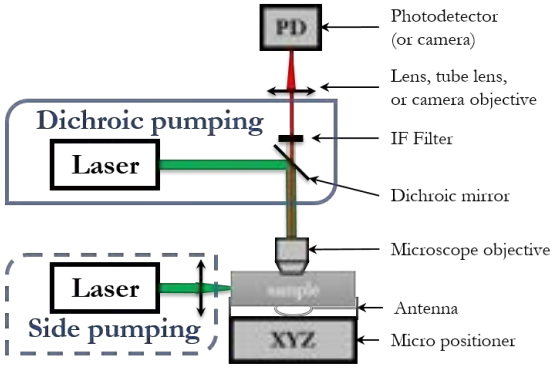

FIG. 4. Schematic of a simple OMDR setup.

1. Light detector and imaging mode

The choice of the light detector is probably the most impacting point in the development of a new setup. It is governed by two main aspects:

a. Single-pixel vs. wide-field imaging — In the former case, a photodetector is sufficient, with appropriate filters placed in front of it to discriminate the signal of interest from the scattered laser light and the possible background luminescence from ODMR-inactive centers[85]. At the cost of small loss of transmitted power, spatially filtering the luminescence signal through a confocal pinhole or an optical fiber reduces the out-of-focus background and collection area (see Fig. 5). If imaging capability is desired it can be obtained by confocal scanning (see II A 5 and Fig. 5).

For wide-field imaging, a pixel array (camera) is required in combination with a large and homogeneous illumination area. Comprehensive reviews about wide-field imaging in the particular case of NV centers can be found in[86–88]. Besides, accordingly to the specific experiments, different cameras (*e.g.* CCD or a CMOS) can be preferred[89].

b. Strength of optical signal — It depends on the number of luminescent centers or molecules being addressed, their individual quantum yields and the collection + detection efficiency. For the study of single or few emitters, a digital photon counter (d-PC) is necessary, such as a reverse-biased avalanche photodiode operated in Geiger mode or a superconducting nanowire detector. d-PCs generate electrical pulses (*e.g.* TTL) upon photon absorption with a quantum efficiency that can exceed 80%, allowing for the study of photon fluxes down to sub-kHz level, limited by the dark count rate of the detector.

For measurements on large ensembles, d-PCs typically saturate at count rates of few tens of MHz (*i.e.* few picowatts at visible wavelengths). Above that analog photodectors (a-PDs) can be used, such as amplified or avalanche photodiodes. In a wide-field configuration with a weakly emitting system, particularly sensitive cameras are required such as Electron Multiplying CCD (low noise) or phosphorus intensified camera (gated).

To enhance the sensitivity in under significant background signal, one can modulate and demodulate the ODMR signal (*e.g.* through the applied MW frequency) with the help of a lock-in amplifier[90]. Such methods can be of great help in the context of biosensing where background emission is strong[39]. For wide-field imaging, the recently developed arrays for lock-in detector[89] may find numerous applications in the upcoming years.

2. Optical components and alignment

When addressing individual emitters, one of the most important parameters is the microscope objective numerical aperture (*NA*) defined as $NA = n \sin\theta$, with n the refractive index of the immersion medium and θ the half cone angle of collection. For one, for isotropic emission pattern, it limits the fraction of collected to emitted light to:

$$\eta < \frac{1}{2}(1 - \cos\theta) \tag{1}$$

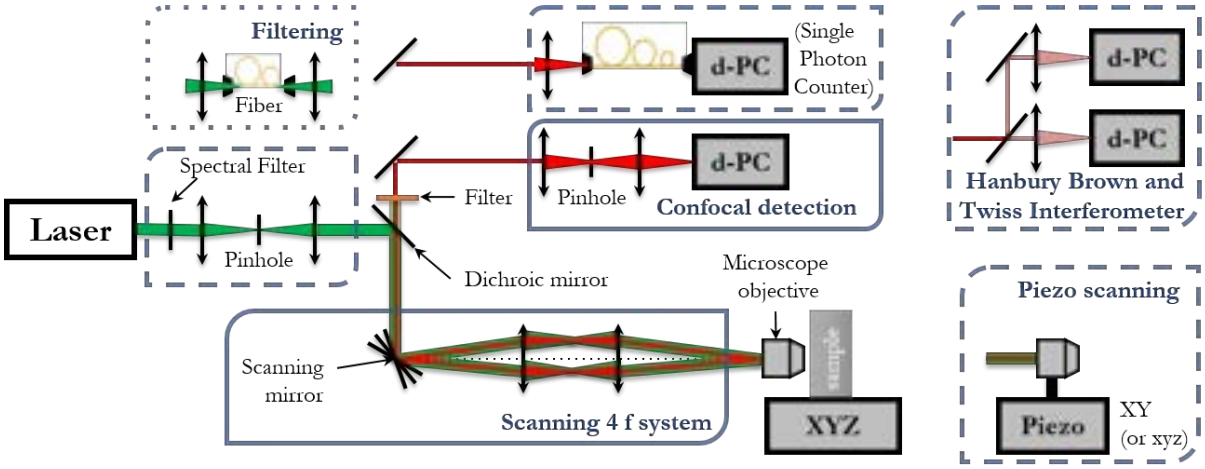

FIG. 5. Schematic of a typical home-build confocal microscope used for low light ODMR experiments. The collimated beam from the laser is spectrally filtered (to remove broadband spontaneous emission) before being reflected on the dichroic mirror and focused on the sample using a high NA objective lens. Photoluminescence is collected by the same objective, passes through the dichroic mirror and an interference filter (band-pass or long-pass) to reject the excitation light, and is optionally spatially filtered using a confocal pinhole or an optical fiber before its intensity is measured by the detector. In order to scan the sample both a scanning mirror or a piezo stage can be used. To study single emitters, a Hanbury Brown and Twiss interferometer can be added.

with $\cos\theta = \sqrt{1-(NA/n)^2}$.

Through diffraction, it also limits the achievable resolution r_{min} defined as the minimum distance at which two objects can be distinguished. As commonly determined by the Rayleigh criterion:

$$r_{min} = \frac{r_{Airy}}{2} = 0.61 \cdot \frac{\lambda}{NA} \tag{2}$$

where λ is the wavelength of the optical source and r_{Airy} the radius of its diffraction pattern on the sample. Similarly, the axial (depth) resolution is set by:

$$z_{min} = 1.4\frac{\lambda n}{NA^2} \tag{3}$$

A larger NA is usually obtained at the cost of a smaller working distance. As a good compromise, an air objective with NA up to 0.9 can offer a working distance of 1 mm.

In contrast, in a confocal setting, the magnification M_{obj} of the microscope objective bears no direct relation to spatial resolution and collection efficiency. It matters however for the design of the excitation and collection optics as well as in the case of wide-field imaging on a pixel array.

To achieve a spatial resolution limited by Abbe's diffraction and avoid unnecessary light loss, care should be taken to the following aspects. Firstly, the excitation beam diameter Φ should match or exceed the back aperture diameter of the microscope objective given by:

$$\Phi = 2f'_{obj}\tan\theta \tag{4}$$

with $\tan\theta = \frac{NA/n}{\sqrt{1-(NA/n)^2}}$, $f'_{obj} = \frac{l_{tube}}{M_{obj}}$ the effective focal lens of the microscope objective, l_{tube} being the tube lens as defined by the microscope supplier (*e.g.* 180 mm for Olympus, 200 mm for Nikon and Mitutoyo and 165 mm for Zeiss).

Secondly, the confocal pinhole of radius r_{hole} (or optical fiber of numerical aperture NA_{fiber}) has to be chosen to match the diffraction pattern of the photoluminescence beam on the pinhole (or fiber). When the image is sent to infinity after the objective the total magnification up to the pinhole (or fiber) equals:

$$M_{tot} = M_{obj} * M_{lens} = M_{obj}\frac{f'_{lens}}{l_{tube}} \tag{5}$$

where f'_{lens} is the focal length of the lens used to focus on the pinhole. So to provide good confocal resolution while avoiding significant optical loss, r_{hole} can be chosen to match the radius of the Airy diffraction pattern:

$$r_{hole} = 1.22 \times M_{tot}\frac{\lambda_{PL}}{NA} \tag{6}$$

Here, λ_{PL} refers to the wavelength of the photoluminescent signal. The pinhole can also be chosen smaller. This would enhance the resolution (*e.g.* reduce r_{min}) by a factor down to $2/3$, at the cost of more optical loss.

If an optical fiber is used instead, its numerical aperture can be taken as:

$$NA_{fiber} = \frac{NA}{M_{tot}} \tag{7}$$

In those cases, either the focusing lens, the pinhole or optical fiber can be changed to obtain the desired spatial filtering. Further details about the basics of confocal microscopy can be found in[91]. Finally, many efforts have been devoted to surpass the diffraction limit in ODMR using super-resolution techniques such as stochastic optical reconstruction microscopy (STORM) and stimulated emission depletion (STED) microscopy[92,93].

3. Light source

For the most studied ODMR systems (Sec. I C), the optical pumping can be performed off resonance. Consequently, there is no stringent requirement on temporal coherence and linewidth of the light source, so that even a white-light LED can be employed, as long as suitable filter sets are used to prevent leakage of excitation light into the detector. Transverse spatial coherence (single mode emission) is however required in a confocal configuration in order to obtain a diffraction-limited spot size at the focus. As shown in Fig. 5, a spatial filter (pinhole or mono-mode fiber) can be introduced in the excitation path to improve transverse coherence. In this case, and using large NA, optical powers of milliwatts or less are often sufficient to saturate the emitter. Therefore, commercially available solid state lasers are a great and affordable option. Optionally, neutral density filters allow to adjust the power incident on the sample while maintaining the laser at its optimal operating power. In the wide-field configuration, the laser power is diluted over the entire area of interest, requiring high power lasers up to watts level.

In all cases, temporal fluctuation in laser power represents the main source of technical noise, which can be mitigated by adding a feedback control loop or monitoring laser power in real time through a second detector. Other forms of technical noises related to pulse measurements are discussed in Sec. II C.

4. PL digitization and visualization

Depending on the type of signal coming from the photodetectordifferent approaches to measure the its intensity are used.

Analog photodetectors (a-PDs) deliver an electric signal proportional to light intensity (temporally averaged over a given bandwidth) that can be visualized directly on an oscilloscope for both continuous and pulsed measurements. Alternatively, a computer interfaced acquisition card that embeds an Analog to Digital Converter (ADC) can be used. In this context, the most relevant features of these data acquisition cards (DAQ) are the number of input and output channels and the maximum sampling rate. The sampling rate sets an upper limit to the the fastest dynamic that can be measured under analog acquisition. While the oscilloscope sampling rate can be chosen up to the GHz range, the DAQ analog inputs are often limited to a few MHz. It as also to be noted than modern oscilloscopes can be interfaced on a computer for direct collection of the data temporally stored in the oscilloscope (see Sec. IV A). In case of pulsed acquisition (see Sec. II C) averaging over several repetition is needed to obtain sufficient signal to noise ratio and/or to reduce the communication bandwidth requirement with the computer. Consequently, it demands a sync pulse for each repetition and limits the averaging strategy to the *NP* method described in Sec. III D.

Digital photocounters (d-PCs) deliver nanosecond pulses (*e.g.* TTL) with sharp rising edge. In such case, the use of a computer becomes almost unavoidable. Conventionally, a time tagging instrument or counter (*e.g.* from Swabian instruments or PicoQuant) provides time resolution down to picosecond range, below the typical timing jitter of the detector. ODMR however, rarely involves that fast processes. Such a time precision can then become a disadvantage as the instrument buffer becomes more rapidly saturated by the recorded time tags.

Alternatively, as discussed in Sec. III A, DAQ cards also include general purpose timers/counters that can be used for photon counting with time resolution up to twice their internal clock rate, up to two orders of magnitude higher than their analog inputs. If one needs higher temporal resolution, for example to resolve the PL lifetime (see Sec. V), a field-programmable gate array (FPGA) can be used as a cost effective alternative to time-tagging instrument, but it requires dedicated programming skills.

Finally, in the case of a wide-field configuration, the camera conventionally embeds its own ADC and directly delivers a digital image to the computer. In such cases, however, acquisition rates are at best up to hundreds of hertz, often too slow to resolve the pulse dynamics. When pulses cannot be isolated from the each others, the averaging possibility is limited to the *NP* method described in Sec. III D.

5. Scanning in a confocal microscope

In a confocal microscopy configuration, locating individual emitters or mapping an area requires scanning the focal spot over the sample. Two possibilities arise:

- The sample or the microscope objective is mounted on an *xy* (or *xyz*) piezo-based nanopositioning stage so as to scan their respective position. In such case, the range is often limited by the stage itself from a few tens to a couple of hundreds of micrometers. If moving the objective, the field of view can also be limited by the shift of its back aperture with respect to the excitation and collection beams.

- The optical beam is angle-scanned by means of a 2-axis oscillating mirror and a $4f$ relay lens system. In such case, the field of view can be chosen by the $4f$ lenses and is ultimately limited by the field number of the microscope objectives.

While the first method is significantly less bulky, the second option is typically more affordable and offers a faster scanning rate. It can also offer the flexibility of changing the objective to adjust the field of view with respect to the resolution. Note that stepper motors and slip-stick piezo stages have bad repeatably: for accurate mapping and positioning, closed-loop positions have to be privileged. We also warn that magnetic materials should be avoided, in particular in the sample stage. In either case, controlling the scanning device requires a computer program and a DAC interface. Such functions are often provided via the aforementioned DAQ cards.

Apart from the essential components described in the previous paragraphs, the setup can be improved to allow addi-

Component	Key specs	Ex. of Brand (and model)	Price (€)	Sec.
Light source	wavelength intensity stability transverse coherence power (for wide-field) intensity modulation option	any diode laser with TEC Coherent (OBIS 532 nm) Labs-electronic (DLnSec 520nm) *Cobolt (06-MLD 515 nm)*	$\sim$ 3k-7k	II A 3
AOM + RF driver	diffraction efficiency switching time (rise/fall)	Gooch & housego (AOMO 3350-199) *AA Opto Electronic (MT350-A0.12-xx)*	$\sim$ 4k	II C
Microscope Objective	numerical aperture working distance Immersion medium (air, oil...)	Nikon, Leica, Zeiss, etc. *Mitutoyo (0.6NA 1.3mm WD)* *Olympus (LMPLFLN 50X 0.5NA)*	$\sim$ 500-5k	II A 2
Dichroic mirror and **fluorescence filter**	cut-on wavelength absorption losses extinction outside transm. band	depending on the ODMR system Semroc, Thorlabs, Chroma. etc.	$\sim$ 100-500	II A 2
Light detector **Analog (a-PD)**	wavelength range bandwidth noise equivalent power	Newport *Thorlabs (APD410A/M)*	$\sim$ 1k-2k	II A 1
Digital (d-PC)	quantum efficiency dark count rate timing jitter	IDquantique (ID100), (ID120) *Excelitas (SPCM-AQRH)*	$\sim$ 2k-8k	
Camera	Pixel size/number Repetition rate, Gating Quantum Efficiency, readout noise	Thorlabs, UEye Andor, Princeton instruments	$\sim$ 500-1500 $\sim$ 2k-20k	
Piezo stage or **scanning mirror**	scanning speed resolution, repeatability travel range Closed vs. open loop	Thorlabs (GVS212/M) *MadCityLab (Nano-3D200)* *Newport (FMS-300)*		II A 5
MW source	frequency range phase noise sweep rate power	Wainvam (Wainvam-e1) Anritsu (MG3691c), Agilent (n9310a) Keysight (M9384B) *Rohde&Schwarz (SMB100B)*	$\sim$ 500-50k	II B
MW amplifier	frequency range gain and maximal power	*MiniCircuit (ZHL-16W-43-S+)*	$\sim$ 5k	II B
MW antenna	field intensity bandwidth spatial homogeneity	Ω-shaped antenna[94] wire loop, straight wire *Sasaki et al.*[95]	< 10	II B
MW switch	insertion loss switching time (rise/fall)	Minicircuit ZFSW-2-4, Minicircuit ZASWA-2-50DRA+,		II B
Acquisition card (DAQ)	maximum ADC sampling rate number of i/o channels	Keysight-U2300A *National Instrument (PCIe-6363)*	$\sim$ 3k-7k	II A 4 II A 5
Pulse generator	minimum pulse width number of channels max. number of pulses	Spincore (PulseBlasterESR-PRO) Zurich Instrument *Swabian Instrument (Pulse streamer 8/2)*	$\sim$ 4k	II C
Time-tagger	minimum bin width dead time timing jitter	PicoQuant (PicoHarp300), IDquantique (ID900)	$\sim$ 3k-10k	II A 4

TABLE II. Necessary equipment for a confocal ODMR instrument, with remarks and examples of suitable providers. The cells in gray color highlight specific equipment for pulsed experiments. In italic is what we used in our own NV setups.

tional characterization features. For example, sending the luminescence to a spectrometer allows to verify its origin and to quantify the amount of background emission (for example, for NV centers, emission from NV^0 is detrimental to the contrast). Moreover, to confirm that a single emitter contributes to the signal, a Hanbury-Brown and Twiss (HBT) interferometer can be used to measure the autocorrelation function[96–98].

B. Microwave instrumentation

The manipulation of electron spins requires MW radiation. According to the targeted spin resonances the MW source should have an appropriate frequency range (See Table I). Also, the phase (or frequency) noise of the source can be the limiting factor when studying highly coherent spin transitions. While a Variable Crystal Oscillator (VCO) can be used as a very cost effective solution, tabletop MW generators such as from Rohde & Shwartz or Anritsu are often preferred in metrology and high-resolution spectroscopy for their spectral purity and power stability. A key specification for CW-ODMR is the dwell time in frequency sweep, which affects the acquisition time. MW powers above 30 dBm that can be achieved with standard MW amplifiers. An insulator should be placed after the MW source and/or the amplifier to prevent back reflections from damaging the instrument.

MW pulses can be carved out of a CW MW source using external switches. Some MW generators may also directly embed an internal switch, which typically offers better performance to measure coherence times less than 100 ns due to lower phase noise between pulses. Furthermore, the MW source must be capable of frequency modulation (FM) for lock-in type measurements. Compatibility between the various MW components must be carefully examined in order to ensure a good match.

The MW radiation is delivered to the sample by MW antennas. Working with ensembles may require spatially homogeneous MW amplitude over several hundreds of μm^2. Several designs focusing on optimizing their field intensity and spatial homogeneity can be found in[94,95,99–101]. Particularly, a trade-off needs to be found between the power conversion to the MW magnetic field (Rabi oscillation frequency), the area of field homogeneity, and the bandwidth of the antenna (important when bias magnetic fields are applied to split the resonances). When spatial homogeneity is not essential, *e.g.* when working with a single spin, a small wire loop or straight wire can serve as MW antenna[102].

C. Pulse generation

For time domain measurements (such the ones described in Sec. I D) a pulse generator must be included in the setup. While a minimum of two output channels is required to control both the MW and the laser, more channels can be useful for synchronization or for more versatile pulse schemes (such as rotating the spin around different axes on the Block sphere, or driving with multiple MW frequencies at once). It is also important that the pulse generator can to provide a minimum pulse length significantly shorter than the minimum coherence time to be measured. To allow multi-pulse protocols (*e.g* for Ramsey fringes), it is also essential that it can fire more than one pulse in each channel after a single trigger.

Two different options are available to produce optical pulses, starting with acousto-optic modulators (AOM). For a wide-field illumination, special care should be taken about the maximum optical admissible beam intensity to prevent any damage of the device. This is to be considered together with the desired rise and fall times, since all those parameters depend on the beam diameter on the AOM. As a handy alternative, laser diodes may embed pulsing capabilities. Unfortunately, overshoot can be present at the beginning of the pulse and depend on the preceding off state duration (through thermal relaxation). It may cause measurement artifacts, in particular when the repetition rate of the laser is varied, like in T_1 measurement (see Sec. I D). While post treatment mitigation methods are presented in Sec. V C, the use of an AOM reduces such artifacts.

D. Bias magnetic field

Several applications require a bias d.c. magnetic field and precise controls of its strength and orientation, which allows to tailor the system eigenstates so that they are most susceptible to the field of interest[103,104]. For example, when NV centers are used for magnetometry and temperature sensing, a bias axial magnetic field often allows to improve the sensitivity[42,105,106]. In addition, applying a field parallel to the quantization axis of the proper magnitude allows to work in specific level configurations such as at the ground state or excited state-level anti-crossing (GSLAC or ESLAC)[107]. Cross-relaxation conditions between different spin systems can be matched by properly tuning the magnitude of an axial magnetic field[108,109]. These configurations can be particularly relevant in the context of all optical sensing[108,110] or spin polarization[111]. Finally, a transverse magnetic field can be relevant in specific situations, *e.g.* for electrometry[103].

Different options are available and reported in literature to achieve this:

- Place a permanent magnet on a micrometer stage[105,112,113]. Controlling the direction, uniformity and intensity of the field can be challenging. Using a pair of permanent magnets mounted on a rotation stage can be helpful for taking advantage of the symmetry of the system. Fine calibration is required for precise magnetic field alignment and repeatability.

- Design a system of three Helmholtz coils, each addressing one axis[114,115]. This approach requires more initial efforts, but leads to higher precision and control. It allows to generate a bias field in any possible direction and to swiftly switch between different bias fields. In[116] a useful numerical model to simulate the magnetic field in the center of the coils for varying parameters can be found. Moreover, note that if the bias field needs to

be modified during the measurement (as for example in real time electrometry[41,117]), this approach is particularly convenient.

- Hybrid solutions, matching the specific application requirements[110,117–119]. It is often not necessary to generate a bias field in any possible directions. Simpler systems compound of one or a pair of Helmholtz coils and permanent magnets are often sufficient. Placing the sample on a rotation stage can offer more convenience and versatility.

To conclude this Section, we refer to Table II that summarizes hardware requirement for a typical room-temperature confocal ODMR setup.

III. CONNECTION AND SYNCHRONIZATION

We previously mentioned that the visualization of ODMR signals can be either performed on an oscilloscope, or through an acquisition card on a computer and we described when the second option is necessary. Here we will overview how to connect and synchronize each laboratory equipment with one another in either case, focusing on four typical measurements in ODMR.

A. Photon detection

As mentioned in sec. II A 4, two main types of detectors (analog photodectors, a-PD vs. digital photon counters, d-PC) can be employed depending mainly on the signal intensity. The required connections for each case are illustrated in Fig. 6.

On the one hand, the analog signal coming from an a-PD, can be measured either directly with the help of an oscilloscope or on a computer after digitization via DAQ. In the latter case, the a-PD is plugged to an analog input. The analog acquisition is limited to the clock frequency of the ADC, f_{ADC}, such that the temporal resolution is $T_{Sampling} = 1/f_{ADC}$. For example, in the case of the NI-6364 card and for single channel, $T_{Sampling} = 0.5\,\mu s$, increased to $n_c \times T_{Sampling}$ when n_c channels are used.

On the other hand, the output of a d-PC is a train of pulses (*e.g.* TTL), each corresponding to one detected photon. A DAQ can be used to measure this signal. Commonly, one of its internal counters is configured to count the number of received photons through one of its PFI (Programmable Function Input). The count is then periodically stored in the DAQ buffer and reset. As a result, the number of counts per interval is obtained. In such a case, the sampling rate can be similar to analog signals.

In order to increase the temporal resolution, which is most desired in pulsed measurements, three counters of DAQ can be used for time tagging. Two counters are set at a high data rate as inputs to count the arriving signal from the d-PC and sync signal which triggers the acquisition. The third counter is set as output and it generates a periodic TTL signal to internally reset the other two. Their count are then saved in the buffer after receiving the TTL reset signal. The reset signal determines the temporal time-tagging resolution. Knowing the relative time difference between sync and signal, the averaged temporal signal can be reconstructed.

Alternatively, the role of the clock and the d-PC pulses can be inverted.The count is then increased by one at each period of the clock, while each photon, at the instant it is detected, triggers its storage to the buffer. This results in a list of time-stamped photons. At the cost of more information saved, which can slow down the computer, this architecture can achieve a better time resolution. With the same NI-6363 card considered above, one can achieve the temporal resolution of $T_{Sampling} = 1/(2 * f_{counter_{clock}}) = 5\,ns$; the factor 2 accounts for both rising and falling edges being counted.

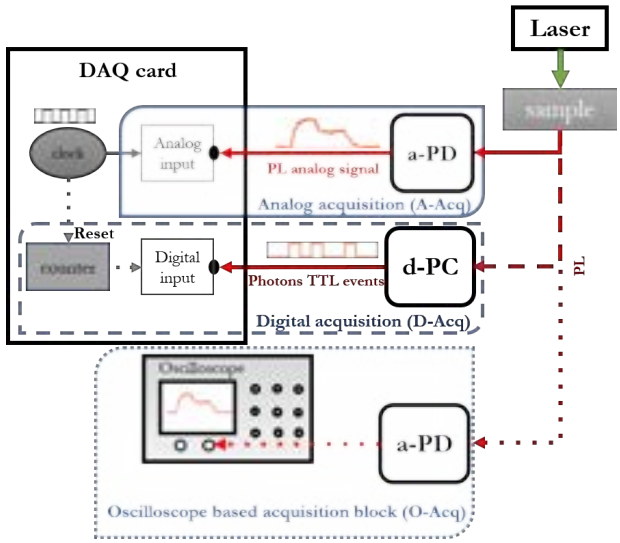

FIG. 6. Hardware connections for monitoring a photoluminescence signal. The solid and dashed/dotted lines indicate the three hardware alternatives. The green color refers to the pumping beam and the red to the sample photoluminescence (PL). DAQ card internal connections are shown in gray. The analog, digital and oscilloscope-based acquisition blocks introduced here, are also used in Fig.s 7, 8, and 9 along with the same conventions.

B. Confocal scanning

In confocal microscopy, a scanning device (such as a piezo stage or a scanning mirror) is controlled while the sample PL is monitored. Synchronizing the two allows to attribute each pixels its corresponding PL intensity creating an image. As illustrated in Fig. 7, these controls and PL monitoring are commonly performed with a DAQ card in which an analog output is used for each spatial axes $(x), (y)$ and (z). The measurement is performed by generating a sync signal of frequency f_{sync} in the acquisition card and three step-ramp functions ranging from the lowest to the highest voltage are sent to the con-

trol ports of the scanning device. Each sync period therefore corresponds to a specific position of the scanning device for which the PL is collected. The sync frequency and order of the generated step ramp functions are eventually used to build the PL image.

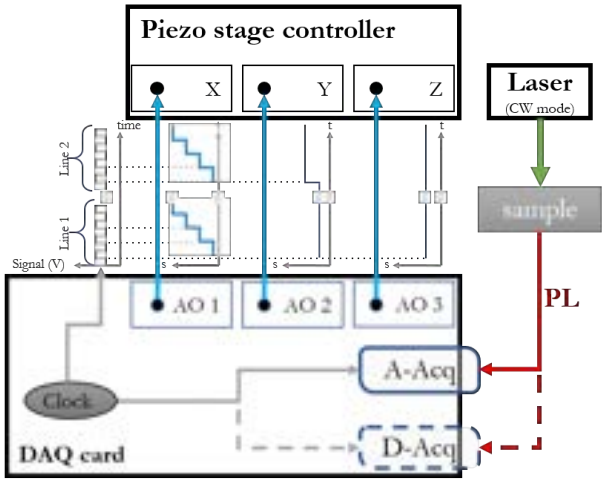

FIG. 7. Hardware connections and synchronization links for confocal scanning. The analog and digital data acquisition blocks are introduced in Fig. 6.

C. CW ODMR

Continuous wave ODMR spectra are measured in a similar way, with the difference that the sweep is applied on the MW frequency instead of the beam (or sample) position. Each optical intensity must be attributed to the corresponding MW frequency. As described in Sec. I D, the plot of the PL versus MW frequency mirrors the magnetic resonance spectrum. As reported in Fig. 8 the DAQ sends a TTL sync signal to the MW source and triggers frequency change while the corresponding PL signal is recorded simultaneously.

In case of using an oscilloscope for acquisition, the MW source, set in frequency modulation mode, becomes the synchronization master. It sends either a sweep or a TTL signal with the same period to a second input of the oscilloscope to trigger at the begining of each sweep. The horizontal temporal scale of the oscilloscope can then be adjusted to display the PL as a function of the frequency. In the case of using a VCO, the frequency has to be set by an external voltage source, such as generated by a DAQ. The visualization on an oscilloscope can be performed in the same way.

Typically, there are two modes to change the microwave frequency: sweep and list. In the sweep mode, the minimum and maximum frequency and the step size are defined. As the MW generator receives a TTL signal, it changes the frequency by the defined step. In the list mode, the list of frequencies are previously stored in the generator, then as a TTL signal is received, the frequency is changed to the next one in the list. The list mode allows to perform random sweeping of the MW frequency mitigating problems such as hysteresis due to frequency-dependent MW heating through the antenna resonance. In practice, the acquisition speed of a CW-ODMR spectrum is limited by how fast the MW generation hardware can switch the output frequency. This values is for example around 1 ms minimum per step for R&S SMF100A.

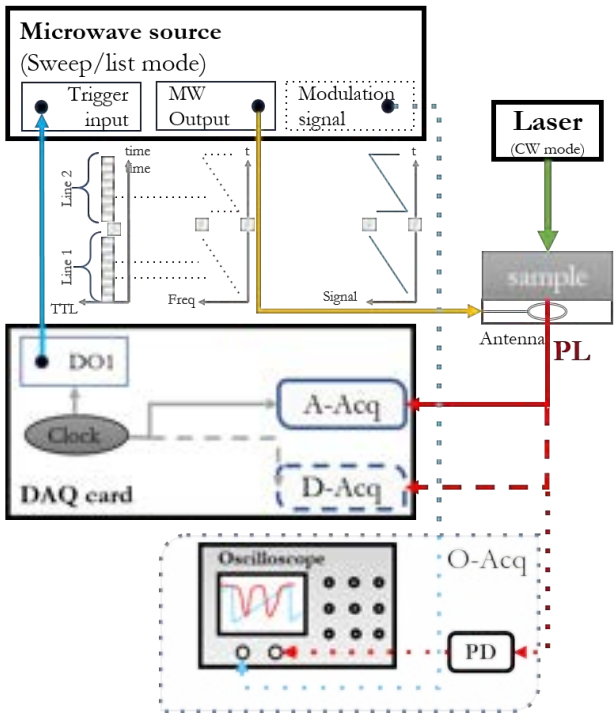

FIG. 8. Hardware connections and synchronization links for CW-ODMR, MW connections are shown in orange. Other conventions are the same as in Fig. 6.

D. Pulsed measurements

As depicted in Fig. 9, pulsed measurements require synchronizing the laser and MW pulses with the optical signal acquisition. A pulse generator sends a TTL signal to command the laser and MW output switch. An additional TTL signal is also generated within the pulse generator to trigger the acquisition and set the time reference for each measurement. This signal is sent to the DAQ or oscilloscope. For each data point of a pulsed experiment, the optical signal is analyzed against the change of one variable (*e.g.*, duration of the MW pulse or wait time between MW and laser pulses, see Sec.I D).

Averaging strategies — We discuss two different options, where $i \in \{1;P\}$ labels the value of a parameter (*e.g.* waiting time) to be swept among P values and N is the number of repetition over which the signal is to be averaged.

- A first averaging method is denoted as "NP", where each i^{th} pulse sequence is individually repeated N times, before moving to the next parameter value from the 1^{st} to the P^{th}.

- In the second one, denoted as "*PN*", a full series of P sequences (consisting of $P+1$ optical pulses since the first only serves as initial polarization)is sent at once while the PL is recorded. This sequence is then repeated as N times to reach the desired signal to noise ratio. In this method, a slow varying noise similarly affects all signals corresponding to all parameter values, and is therefore averaged out. It also allows to monitor the signal to noise ratio improving over the successive repetitions. However, it demands sufficient time resolution to isolate signals from each pulse sequence making it hardly compatible with the use of a camera. It also requires digitizing and storing the full sequence at once, which also limits the use of an oscilloscope (see Sec. II A 4).

Synchronization strategies — In either cases, two distinct synchronization methods are possible:

- 'Sync method 1': Only two TTL sync pulses are generated, at the start and at end of each series of N (or P) sequences.The incoming optical signal is continuously recorded between the initial and final pulses according to the sampling rate. The position of each pulse is then calculated by software (see Sec. V C). This cannot be done when using an oscilloscope.

- 'Sync method 2': A TTL pulse can be sent at the beginning of each pulse to be either timestamped by the counter with a DAQ card or used to trigger the oscilloscope.

Fig. 9b depicts two out of the four possible combinations of averaging and synchronization strategies in the case of a Rabi oscillation measurements.

Implementation with a DAQ card — The implementation of aforementioned methods with an NI card can be elaborated based on the type of the acquired signal.

- In the analog case, the a-PD signal is sent to an analog input channel of the DAQ card. As discussed in section III A, the ADC captures and save the analog signal into the buffer until it is read out. With 'Sync method 1', the generated sync pulses are transmitted to another analog channel of the DAQ card and the acquisition starts as soon as it receives a sync pulse. As a consequence, the optical signal is recorded even when the laser is off. Identification of each pulse then requires post-processing as described in Sec. V. With Â´Sync method 2', the generated sync pulses are sent to a digital channel of the DAQ card. The channel is adjusted to acquire the pulses during the laser pulse windows using start edge trigger and pause trigger protocols of the DAQ card.

- Acquiring data from a d-PC, however, demands time-tagging as described in section III A. Similarly, the 'sync method 1' records all the photon received. the pulses are found and reconstructed by post-processing. With 'sync method 2' the trigger signals are time-tagged and mark the beginning of each pulse.

One chooses the synchronization method depending on hardware limitations and desired averaging strategy discussed above.

IV. QUDI, AN OPEN-SOURCE INTERFACE FOR ODMR EXPERIMENTS

As discussed in Sec.s II and III, the use of a dedicated software can be necessary to control a confocal microscope or deal with photon counting. It can also automatize the control of ODMR instruments to speedup the measurements and ease their reproducibility, be it for fundamental studies or application development. Ideally, the software interface should allow dealing both with single photon counters in low light conditions and with analog photodetectors, processing confocal and wide-field images, and freely combining different measurement parameters and methods.

Several options exist for coding such interface program. On the one hand, mid-level languages such as C++ or FORTRAN, down to the lower-level ones such as assembly, offer the best possibilities to optimize computer resources. They are often the best option for demanding computational physics and simulations, artificial intelligence related research, or for processing of complex or voluminous data[120]. On the other hand, higher level programming languages, such as Python or Java, greatly facilitate design, development and maintenance of codes. They also ensure better portability between different hardware configurations. They are therefore particularly appropriate for interfacing laboratory experiments[121,122]. A comparison between programming languages including C, C++, Java and Python can be found in[123].

Among others, Labview (for Laboratory Virtual Instrument Engineering Workbench), a proprietary programming environment developed by National Instruments[124], offers a graphical diagram coding style making it more intuitive to newcomers in programming. Moreover, it allows to easily interface with laboratory instruments and offers libraries for signal generation, data acquisition and processing which allow to rapidly setup basic experiments. However, when the experimental complexity increases, this graphical programming style can become difficult to handle. It also remains incompatible with versioning and collaborative tools such as Github for sharing codes and subroutine within a community.

In this context, Python, a high-level programming language, offers a great alternative[125]. Coding environments and interpreters being open source, it is particularly popular and used in various domains, including experiment control. It supports versatile and efficient community-developed libraries. Moreover, it offers sufficient level of abstraction to allow portability between computers of different configurations and making it upgradeable to new functionalities, embeds efficient multi-threading and signaling capabilities allowing for parallel operations (data acquisition, processing and display).

In this section we introduce Qudi, an open-source Python code dedicated to ODMR measurements. First presented in[19], it is an open-source collaborative project shared on Github and it benefits from a well programmed Python-based archi-

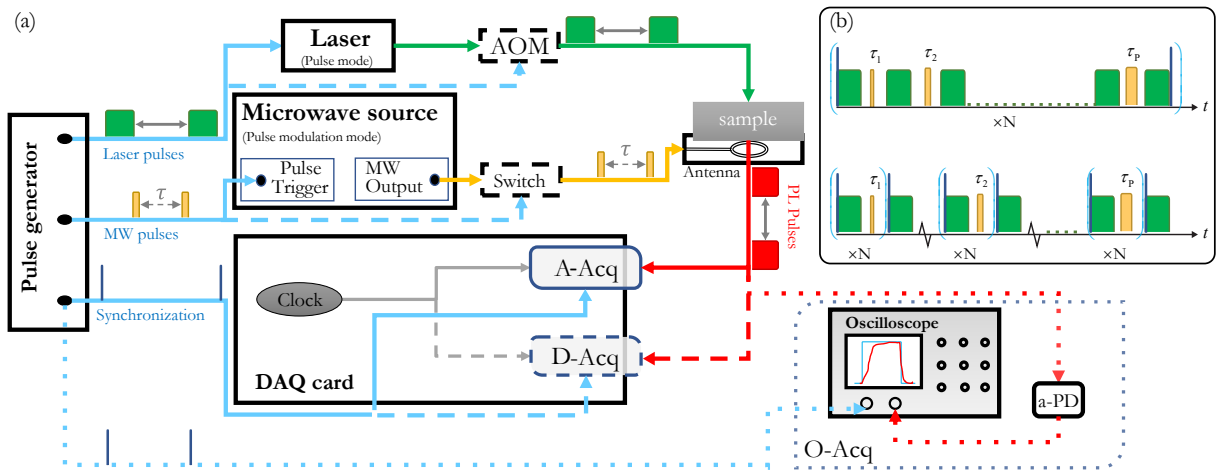

FIG. 9. (a) Hardware connections and synchronization links for pulsed experiments. Solid and dashed lines indicate different alternatives depending on available hardware. (For example, if the laser uses pulsed modulation, the AOM is not required.) (b) Averaging and synchronization strategies in the case of a Rabi measurement. Top: *PN* strategy with 'Sync method 1', Bottom: *NP* method with 'Sync method 2'

tecture. In order to improve its performance and extend its applicability, we added to the original version several features that we present below. After that, we introduce its architecture focusing on the notions that are useful for installing, configuring and using it. It then allows us to guide the newcomer from getting started up to their specific needs including configuration and upgrade for interfacing new instruments.

A. Original and added features

Original Features — Qudi[19,126,127], first released in 2017, embeds modules to perform ODMR experiments, controlling the instruments and handling the data acquisition and their processing on the go. It provides useful tools for interfacing a scanning confocal microscope by controlling piezo-based nanopositioning stages or scanning mirrors and collecting the optical emission signal. Fast imaging (or scanning) is performed by generating beam position sweeps over the sample while acquiring the luminescence in a synchronous manner. Possibilities include in-plane scanning (xy), z-stack acquisitions (so to obtain 3D images), out of plane (xz) or (yz) as well as any other direction cuts depending on the wiring and instrument. Associated to confocal microscope hardware (see Sec. II A), Qudi can be used to locate individual ODMR emitters and automatically track them during an acquisition by interrupting it shortly and re-optimizing the signal, which allows to compensate for sample drift. This feature is particularly interesting when dealing with nanoparticles in a liquid suspension such as in biomedical applications[128,129].

Qudi also allows to efficiently control the different instruments that are necessary to acquire a CW ODMR spectrum and to find the frequency of the spin resonance. Several common analytical curves can be fitted in real time on ODMR data helping to adjust the acquisition parameters and quickly share the results with collaborators.

In addition to the CW ODMR signal, Qudi is designed for the study of spin dynamics with pulse sequences such as for measuring longitudinal spin relaxation curves (T_1), Rabi oscillations, Ramsey (T_2^*) or Hahn Echo (T_2) sequences (see Sec. I D). It can control the pulse generator for triggering laser and MW pulses (see Sec. II C) in a synchronous manner with the collection of the photoluminescence (see Sec. III D). Several tools are available to extract and analyze the pulses on the go and to automatize the setting of experimental parameters, which facilitates long measurement sequences across many different material systems.

Added Features — In its first version Qudi was primarily designed for experiments on single quantum emitters, thus requiring digital single photon counting modules as well as time tagging electronics in the pulsed measurements. In order to broaden its contextual applicability, we added several features.

1. We implemented a direct oscilloscope interface (see Sec. II A 4).

2. We enabled the use of digital inputs of a NI card (or similar DAQ device) as a relatively fast event counter. As presented in Sec. III A, the minimum temporal resolution is can now be down to half the period of the card internal clock, which is often more than sufficient for ODMR experiments. Such using of the same DAQ, often already required to control the confocal scanning and monitor analog signals, relaxes the need for more expensive dedicated time tagging instrumentation.

3. We implemented the two strategies for photon counting presented in Sec. III A.

Module	Original features	Added features
Counting	Analog acquisition Digital acquisition	Acquisition with oscilloscope Faster and analog and digital DAQ acquisition
Confocal	Analog acquisition Digital acquisition	Acquisition with oscilloscope Control with pulse streamer
ODMR	Analog acquisition Digital acquisition	Arbitrary/random MW sweep Acquisition with oscilloscope Acquisition with Spectrometer *Lock-in detection*
Pulsed	Digital acquisition with time tagging device	Analog acquisition with DAQ Analog acquisition with oscilloscope Digital acquisition with DAQ Pulse extraction improved New pulse sequences

TABLE III. Summary of Qudi main features in the original release[126] and in our upgraded version[127]. Features in italic are currently under development.

4. We coded a new logic for the pulsed measurements to avoid storing data directly in the DAQ during the dark time between laser pulses. With respect to the originally programmed one, it enhances the speed of the pulsed measurements acquisition, in either the digital and analog cases, especially for measurements where there is long dark times. This method also relaxes the need for post treatment pulse extraction as described in Sec. III D.

5. We equipped Qudi with the capability to perform pulsed measurements using analog signals (pulsed data could previously be acquired digitally only). This aspect makes Qudi compatible with the study of ensembles of emitters (see Sec. II A 1), and in general with all types of analog photodiode signals.

6. We improved analog acquisition in CW-ODMR by increasing the sample rate per frequency sweep from one to the maximum value, which is given by the ratio of the frequency of the ADC clock and the rate of frequency sweep of the MW source (see Sec. III A). This achieves maximum signal-to-noise ratio for a given measurement time.

7. Further improvement on CW-ODMR has been done by adding an arbitrary/random MW frequency sweep, to minimize the thermal effect of the resonator on the ODMR signal.

8. We extended the ODMR module by adding the option of acquiring the ODMR signal using an optical spectrometer. This module uses a user-specified spectral window and averages the optical intensity over this spectral band for each MW frequency to calculate the ODMR signal. The module can be used, for example, to determine the optimal filter pass band to maximize contrast and signal-to-noise ratio.

9. Finally, with the same goal of improving ODMR acquisition, we are currently developing a lock-in detection scheme. In this method the signal from the lock-in amplifier (*e.g.* Stanford Instrument) is sent to the DAQ and the corresponding demodulated ODMR spectrum is plotted in the software.

The summary of the added features to the Qudi platform is shown in Table III.

B. Main architecture

Qudi is made of different modules that are loaded and connected together by a manager component. The science modules responsible for experiment control are divided into three categories: GUI (graphical user interface), logic, and hardware. As detailed in the following, this division is based on a clear separation of tasks among the categories and offers a reliable and flexible software architecture and simultaneous (multi-threading) acquisition, data treatment and visualization. Importantly, the setting of those modules and the links between them is to be defined in a configuration file. The writing of such a file will be discussed in Sec. IV C 2. The important notion of hardware interface (higher abstraction level of hardware module) is also introduced.

1. Modules

GUI modules — They create an interactive graphical interface which allows the user to control the experiment and to visualize the acquired data. In particular, the GUI allows to start and stop the acquisition, to adjust the experimental parameters (*e.g.* MW power, frequency sweep range, acquisition time...), to save the data and to fit them with pre-defined functions, simply pushing buttons or inserting values into the interactive windows. Changes made in the graphic interface, such

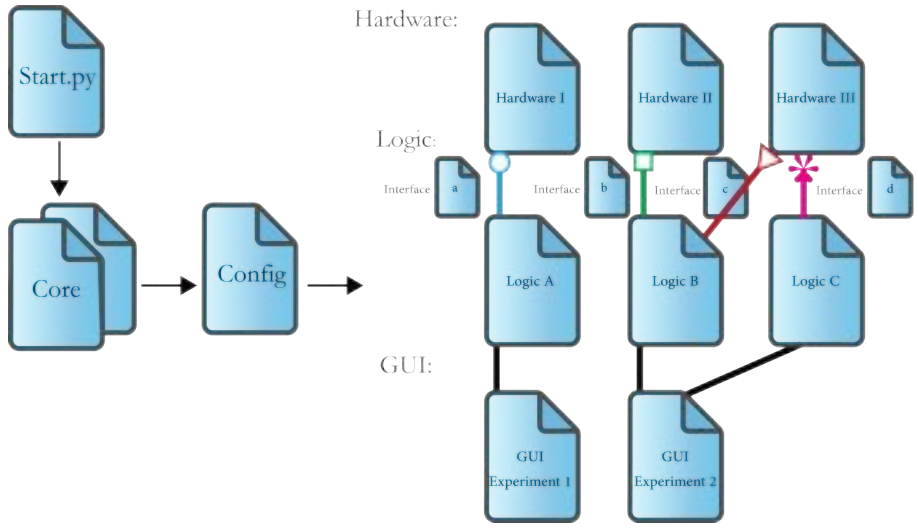

FIG. 10. Qudi modules and software architectures. Running Qudi experiments requires a configuration file created exclusively for one set of experiments. It is accessed by Qudi through core modules while `start.py` is running. Inputs are read from the configuration file and passed to the related scientific modules (GUI, logic, and hardware). Hardware modules are accessed via interfaces as described in the text.

as a pushed button or a modified parameter, trigger a broadcast signal sent to the related logic modules. Although GUI modules offer an intuitive and efficient way to interact with the logic modules, Qudi can also be fully functional without them via the integrated Ipython console or via a Jupyter notebook.

Logic modules — They form the basis of every experiment designed in Qudi. Their main function is to coordinate the different tasks necessary to perform a complete experiment. They serve as a bridge between the two other kinds of modules. On one side they receive the emitted signals from the GUI modules and they send others to the hardware modules to configure the instruments[130]. Conversely, they gather and analyze data coming from the hardware modules and pass them to the GUI modules for display.

Each experiment depends on a variety of generic tasks that are common to different types of measurements. This includes for instance, fitting appropriate curves, saving the data, etc. Therefore, rather than having a single logic module for each experiment performing all these tasks, they are divided in multiple versatile logic modules are implemented. Besides communication with hardware and GUI modules, each logic module can receive inputs from and send outputs to other related logic modules. Note that logic modules are the only ones allowed to talk to modules of the same category.

Hardware modules — The main task of these modules is to allow an effective communication between the logic modules and the specific hardware. Receiving orders from the logic modules, they run the equipment drivers (often provided by the supplier) to act onto the experiment. They also send the output signals of the instruments to the logic modules, to be further analyzed, displayed and eventually saved. Moreover, hardware modules can also work as virtual dummy or mock hardware, emulating the functionality of a real device. This possibility can be very helpful for configuring a new setup.

2. *Hardware interfaces*

Even if a set of instruments have common features for performing similar tasks there is, between different models and suppliers, a wide difference in command structure, grammar and connection methods. In order to handle this complexity, a specific interface is defined for each category of instruments. In the context of object oriented programming, hardware modules are classes that inherit from hardware interfaces. The running of a laboratory equipment consists in defining and operating instances (objects) from the instruments-related classes. The interface therefore consists of a set of functions that each hardware module within the same category must implement. Therefore, each instrument used in an experiment should have its own class compatible with the related interface class in Qudi. This class needs to control the instrument while respecting constraints on its operation as specified in its data sheet. To accomplish this task, the class may use drivers provided by the instrument's manufacturer. Various instruments have already been introduced in Qudi in different categories (such as spectrometers, cameras, MW generators, pulse generators, etc.). However, due to the wide variety of systems, applications suppliers and models available, it may be necessary to add a new device or modify the class for an instrument whose model is slightly different from the one defined in the code. This will be discussed in Sec. IV C 3.

C. Installing and configuring Qudi

To perform an experiment with Qudi, it is necessary to install and tune it for a specific experiment by writing a configuration file. For installing an equipment that is not yet supported, it is also necessary to write the corresponding hardware module class. Once these steps are done, it is possible

to run Qudi, adjust experimental parameters and launch the acquisition through the graphical interface.

1. Installation in an appropriate Python environment

Installing Qudi is rather straightforward from Qudi Documentation's instructions[131]. It can be cloned from the original[126] or our[127] Github. The `conda` environment installers for various operating systems can be found in the folder `qudi\tools`. After installing the appropriate one, the user can execute the program by launching `start.py` in the `conda` environment.

A `conda` environment is a directory for a desired set of `conda` packages[132]. Installing, removing, or upgrading the packages in one environment does not affect the other ones. Therefore, for important coding projects that use many modules and packages such as Qudi, it is preferable to install all the dependencies in a specific environment and launch the program through it to prevent any conflicts with other programs.

Anaconda is one of most popular tools to manage such `conda` environments: it easily allows users to build and switch between them. Python projects, including Qudi, usually include a `.yml` file that lists all the dependencies of the project (for Qudi, it can be found in the folder `qudi\tools`). Anaconda builds the environment directly via this file.

By running `start.py`, Qudi begins by loading the core modules. They are responsible for the primary functions of the process, including reading and loading the configuration file, loading and managing modules, and handling error logging and remote network access. Once the program is executed with no error, the Qudi task manager GUI will open up. Initially, when the user runs the program for the first time, Qudi will configure itself based on the default configuration file, located in the address `qudi\config\example` in the downloaded files. The default configuration file does not need to be connected to any real hardware: it uses virtual dummy or mock hardware, which emulates the functionality of a device, to offer first-time users a demonstration of how different parts of Qudi should look like. However, to do a real experiment, one needs to write the configuration file, as explained in the following.

2. Writing a configuration file

The Qudi configuration file is a text file listing all required modules and their connections. It is written in YAML format, a data serialization language compatible with all programming languages, and provides the software with all the information necessary to configure itself for the desired experiment. To let the program work properly, it is necessary to follow the exact writing style. Inside the configuration file, the modules are listed under the three main categories (Hardware, Logic, GUI). In general, the class name and directory are required for all modules. The other inputs vary by module type. For every hardware module the connection address (*e.g.* IP or GPIB address), and the critical hardware constraints are required. For logic and GUI modules, the connections should be indicated. Figure 11 presents required modules for the four typical experiments described in Sec. III and the connections to be declared in the configuration file.

To avoid users missing any input, all Qudi module codes include examples to be copy-pasted into the configuration file. Other general examples are also provided in the directory `qudi\config\example`. In any case, these have to be adapted to the user's own need and configuration. Besides the specific modules, the Manager GUI and Tray module should always be included in a configuration file. Loading the Tray module, the Qudi icon appears in the system tray: by clicking on the icon, the user can quit the software or bring its main window to the front. The Manager GUI provides access to the core manager class, resulting in the display of the graphical user interface. Through this interface, it is possible to activate or deactivate modules, and switch between configuration files.

3. Interfacing unsupported instruments

Interfacing new equipment is likely the most common upgrade Qudi users may want to perform. As described in Sec. IV B 2, each category of instrument has its own hardware interface whose list can be found in the folder `qudi\interfaces`. In the simpler case, new equipment belongs to an existing category. The task is then to create a new hardware module class inherited from the corresponding interface. Interface classes contain 'abstract methods' in which only the name and inputs are specified. The implementation of the methods belongs to the hardware module classes. There, the interface class should be imported, and the methods specified in the interface should be implemented with the same inputs and names as the abstract methods. This implementation then depends on the device itself and the specific driver given by the supplier. Even if the device does not have a particular functionality defined in the interface class, the corresponding method must still be defined in the hardware class. Yet, it can be passed without any commands.

For interfacing new instruments that do not belong to an existing interface class, the user needs to go deeper in the code to develop it.

4. Running Qudi

When all devices have been introduced to Qudi and all the necessary modules have been listed in the configuration file, we are ready to run the code and perform the experiment. From the manager window it is possible to adjust the different parameters. The results will be displayed in real time in the GUI. There are several fitting graphs, along with further data analysis tools that can be helpful when adjusting experimental parameters or reporting results. Moreover, the pulsed measurement section offers the option of using a predefined sequence, or of building a new sequence of pulses.

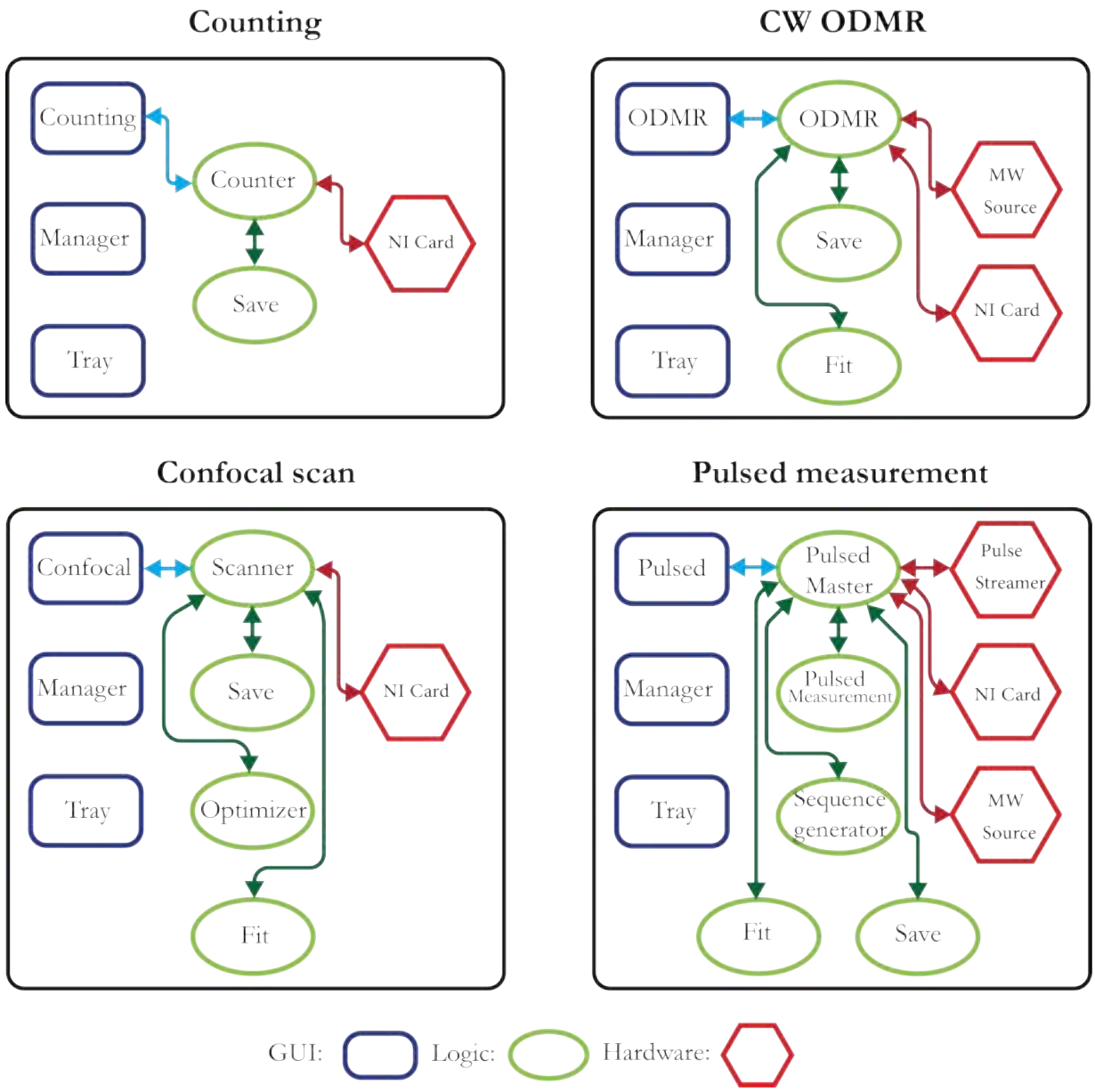

FIG. 11. Block diagrams for the software connections of counting, confocal scan, CW ODMR, and pulsed measurement which needs to be included in a Qudi configuration file.

In the following chapter, we will focus on the characterization of an NV center ensemble to propose some practical advice and discuss good practices when performing typical ODMR experiments with a home-build confocal microscope (see Sec. II) controlled using Qudi.

V. GOOD PRACTICES FOR ODMR MEASUREMENTS: NV CENTER CHARACTERIZATION

As described in Sec. I D the main figures of merit characterizing an ODMR system are the longitudinal spin relaxation time T_1, dephasing time T_2^* and coherence time T_2 (the latter being dependent on the type of echo sequence used to measure it). In this section, we describe the procedure and methods to reliably perform these measurements such as presented in Fig. 3. As an illustration, we characterize a small ensemble of NV centers in bulk diamond using a single pixel detector in a confocal geometry (see Sec. II A 1). While an extensive review on optimizing sensitivity with NV centers can be found in[42], we aim here at providing practical advice on how to easily reach good measurement quality in terms of acquisition speed, contrast and repeatability.

A. Procedure

The sample is first placed in the optical setup and its position adjusted to match the object focal plane of the objective. A confocal scan allows to image the sample and identify the region of interest. At this step, further alignment of the setup to ensure that maximum signal is emitted by and collected from the NV centers is possible. According to the level of brightness of the sample a proper detector (*e.g.* photon counter or analog photodiode) and possibly a neutral density filter are selected. Then, we use Qudi ODMR interface to perform a CW-ODMR scan. The goal of this step is to adjust the bias magnetic field (by monitoring the different resonances in the spectrum) and to identify the resonance frequency that will be used for the following pulsed measurements.

One specificity with NVs is that each center can take one of the four (111) crystallographic orientations of the diamond lattice. Considering the two allowed MW transitions from $|m_s = 0\rangle$ to $|m_s = -1\rangle$ and $|m_s = +1\rangle$, this can lead to eight distinct resonances (that are further split by hyperfine interaction) whose frequencies correspond to the projection of the magnetic field along each orientation. It allows to perform vectorial magnetometry[81,133] with respect to the laboratory basis, even without biased applied fields[134,135]. Certain applications, may require a specific magnetic aligning (see Sec. II D). In this example, we target a bias field such that the Zeeman splitting for at least one NV orientation is different from all other orientations, *i.e* at least one pair of transitions in the spectrum is non-degenerate.

We select a MW frequency resonant with one of these two transitions (corresponding to either $|m_s = -1\rangle$ or $|m_s = +1\rangle$) and perform pulsed measurements to characterize T_1, T_2 and T_2^*. To this end, we move to Qudi interface for pulsed Measurement. Rabi oscillations are first measured to determine the duration of a π pulse which is half the oscillation period. We note in passing that the decay of Rabi oscillations is not simply related to any of the time constants mentioned above because increasing the MW pulse duration reduces is spectral bandwidth and thus progressively filters a smaller set of NV centers among the inhomogeneously broadened ensemble. Since a good estimate of T_2^* can be obtained from the CW-ODMR linewidth (in the limit of low MW powers) it is recommended to use sufficient MW power in the pulse sequences so that the π pulse is shorter than T_2^* in order to efficiently drive all NV centers in the ensemble. The last step consists in applying each of the dedicated pulse sequences to extract T_1, T_2 and T_2^*, previously presented in Sec. I D.

B. CW ODMR

In order to perform CW ODMR with highest possible contrast and narrow linewidth, a compromise must be reached in terms of both MW and laser powers, as illustrated in Fig. 12. While the optical excitation rate must be faster than the $1/T_1$ relaxation rate to ensure that all spins are well polarized, a too high rate can decrease the ODMR contrast by competing with the MW excitation and preventing a large population

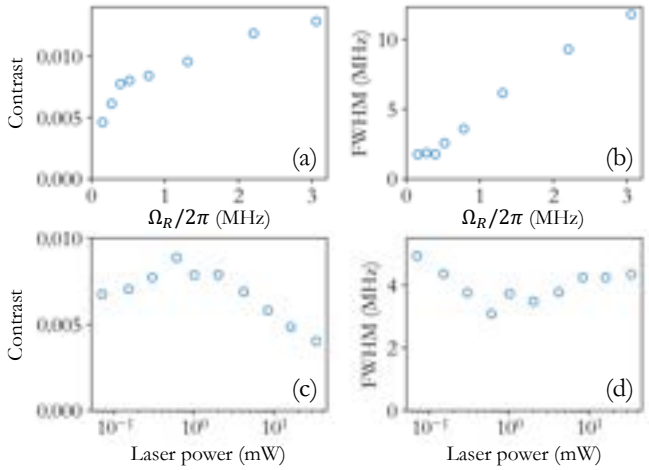

FIG. 12. (a, c) Contrast and (b, d) FWHM of a single resonance in the CW ODMR spectrum, versus (a, b) MW Rabi frequency and (c, d) laser power.

difference between states $|m_s = 0\rangle$ and $|m_s = 1\rangle$[136]. On the other hand, while increasing the MW power first enhances the contrast, it then broadens the resonances through power broadening[76].

As practical guidelines (for NV ensembles) the optimal laser power is the one maximizing contrast and the optimal MW power is the highest power for which the linewidth remain close to the T_2^* limit. For further optimization, the optimum condition for the laser and MW power can be derived analytically using a rate equation approach[76,136].

C. Pulsed experiments

To improve the quality of a pulsed experiment several factors should be taken into account. Some are general to all pulsed protocols, while others are more specific. Common requirements for all pulsed experiments are reliable initialization and readout. Laser pulse duration needs to be long enough to ensure maximum polarization in state $|m_s = 0\rangle$. The characteristic time for spin polarization depends on the optical power and typically ranges from 100 ns to 1 µs. For NV centers, the initialization pulse must be followed by a waiting time, typically 1 μs, to allow relaxation of population trapped in the singlet state towards the ground state $|m_s = 0\rangle$[137]. The characteristic polarization time also impacts the readout phase. Depending on the time resolution of the hardware (see Sec. II A 4 and III A), it can be convenient to reduce the laser power, to polarize the spin slower and be able to resolve it dynamics as in Fig. 13. The duration of the optical pulse needs to be adjusted accordingly.

In the case of 'Synchronization method 1' (see Sec. III D) in which only the beginning and the end of a sequence is triggered, it is necessary to locate each pulse within the entire recorded optical signal. In this case, two standard approaches are implemented in Qudi for pulse recognition. The first uses a threshold value to identify rising and falling edges of a pulse.

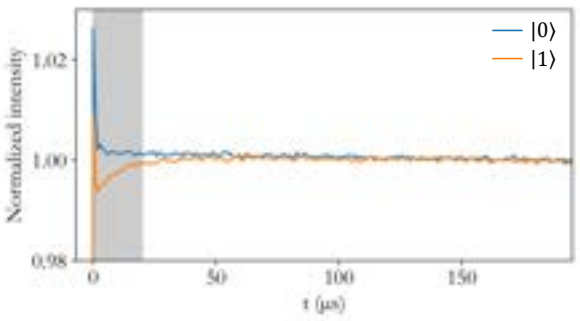

FIG. 13. Normalized luminescence intensity during the readout laser pulse, for spins initialized in state $|0\rangle$ (blue curve) and $|1\rangle$ (orange, using a π pulse between optical pumping and readout), collected with NA 0.65 objective and 35 mW incident laser power. The shaded gray region indicates a good choice of time window for signal integration, yielding high SNR.

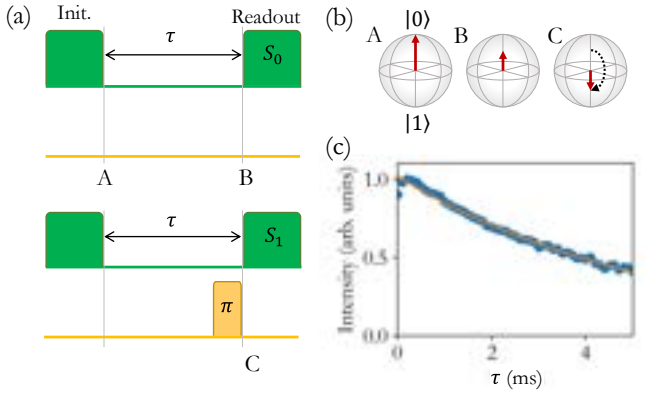

FIG. 14. (a) Pulse protocol for optimized T_1 measurement, with the addition of a π-pulse to extract S_1. (b) Bloch sphere representation of the spin state at times of the pulse protocol indicated in (a). (c) Resulting signal versus delay τ, fitted with an exponential decay (solid line)

The second relies on a convolution of the signal with a Gaussian distribution and takes its first derivative, resulting in a pulse identification signal $S_p(t)$ given by:

$$S_p(t) = \frac{d}{dt}\left[S_r(t) \otimes \frac{1}{\sigma\sqrt{2\pi}} e^{-\frac{1}{2}\left(\frac{t}{\sigma}\right)^2}\right] \tag{8}$$

where t represents the time and $S_r(t)$ is the raw signal acquired during the pulsed measurement; σ is the standard deviation for Gaussian filter. Rising and falling edges of pulses correspond to local maxima and minima of $S_p(t)$. The Gaussian filter allows to smooth the signal and reduces the possibility for spurious pulse detection. This second method is thus generally more robust than the first one. Optimal extraction is achieved by adjusting the parameter σ.

Figure 13 displays the time evolution of luminescence intensity during a laser pulse starting at $t = 0$, for spins initially prepared either in $|m_s = 0\rangle$ or $|m_s = 1\rangle$. The different levels of PL in the two cases and the spin polarization dynamics, are clearly resolved. To obtain a measure of the spin projection along the quantization axis the PL intensity is integrated over an early time window marked as gray shaded area, and normalized to the PL intensity integrated at the end of the pulse (not represented), when spins are polarized again. It allows to compensate possible slow fluctuations of the laser intensity or collection efficiency.

To maximize the signal to noise ratio, the time window should start with the laser pulse, where the PL difference between $|m_s = 0\rangle$ and $|m_s = 1\rangle$ is maximal. If the initial time of a pulse is not properly identified by the pulse extraction method for all pulses in the sequence (*e.g.* due to slow laser rise time), the resulting timing jitter translates into noise on the total integrated signal. In this case excluding very early times of the readout pulse can be beneficial in this case.

Several other sources of noise can affect readout fidelity. Among them, some are spin-independent, for example due to NV ionization and NV- recombination caused by the laser pulse[138,139]. A powerful solution to suppress this kind of noise is to repeat the pulsed protocol but inverse the spin state onto $|m_s = 1\rangle$ just before readout using a π-pulse as illustrated in Fig. 14 [140]. The extracted signals with and without inserted *pi* pulse are labeled S_1 and S_0, respectively. The expectation value of the spin state projection is linearly related to the difference signal $S_0 - S_1$ from which spin-independent common noise is removed. The result of this procedure for a T_1 measurement is illustrated in Fig. 14.

Another important source of artifacts arises when the dark time ΔT between consecutive laser pulses is swept. As mentioned in Sec. II C it can lead to variation in laser pulse intensities over for the entire sequence. In most cases, a simple solution is to keep ΔT constant, adjusting some waiting times before and after the microwave pulses accordingly, as long as $\Delta T \ll T_1$. It is however not possible for a T_1 measurement. Fortunately, the protocol discussed just above allows to partially mitigate such artifact by normalizing the signal by $S_0 + S_1$. Such protocol also allows to extract a relevant signal even when the setup temporal resolution does not allow to resolve the pulse dynamic, *e.g.* when using a camera in a wifefield configuration.

A final knob for optimization of pulsed measurements is in the definition of π, $\pi/2$ and other pulses. The duration of such pulses is in principle extracted from the measured period of Rabi oscillations. However, in practice small deviations can arise, *e.g.* due to not perfectly square MW pulses and fitting errors. It is thus good practice to perform a calibration step. To this end, we use a Hahn echo sequence with fixed delay and monitor the echo amplitude for varying initial, central and final MW pulses. The result of this procedure is illustrated in Fig. 15, where the initial and final pulses are half the central pulse. Every second sequence, we also replace the final pulse with a $3\pi/2$-pulse, to apply the above common noise rejection strategy. The optimum pulse duration corresponds to the simultaneous maximum echo amplitude when the final pulse is $\pi/2$ and minimum when it is $3\pi/2$. This ensures maximum contrast for a T_2 measurement, using the Hahn echo sequence (Fig. 3(d)). The calibrated $\pi/2$-pulse is also used for T_2^* mea-

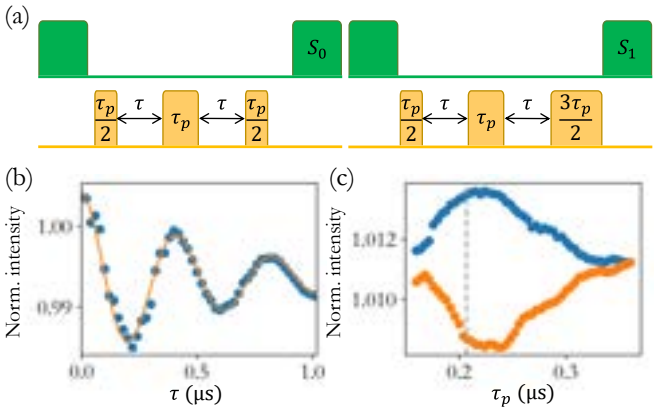

FIG. 15. (a) Hahn echo sequence used for optimization of π and $\pi/2$ pulses. (b) Rabi oscillations with cosine fit (solid line). (c) Echo amplitude versus pulse duration τ_p. The delay is $\tau = 500$ ns. Dashed line indicates the π-pulse duration extracted from fit of Rabi oscillations in (b) which appears not to be optimal.

surement using Ramsey interferometry (Fig. 3(c)).

CONCLUSIONS AND PERSPECTIVES

The preceding chapters provided an overview of currently available hardware and open-source software for ODMR and related hybrid MW-optical measurements. In particular, we showed that a relatively inexpensive acquisition card equipped with analog-to-digital converter, together with our upgrades on the Python-based software Qudi, allow anyone with minimal experimental skills to setup ODMR instrumentation capable of implementing advanced magnetic resonance pulse sequences and addressing individual optically-active spin-systems or large ensembles. We believe that our work will help foster development ODMR studies and applications to sensing and metrology, quantum technologies, and material science, while also making ODRM methods more accessible to non-specialists. We encourage Qudi users to develop new instrument modules and make them available on GitHub to participate to wider openness and collaboration in research. We conclude by mentioning a few envisioned directions for both hardware and software developments in the coming years.

As we have shown, performing ODMR at room temperature without space constraints does not present significant hardware challenges anymore. Yet, implementing similar measurements in confined environments, in ultra-high vacuum or at cryogenic temperatures, can rapidly become much more complex. This may restrict the range of quantum sensing applications, with NV centers or other systems. While optical excitation and collection through free space or optical fiber is usually feasible in such circumstances, it can be challenging to locally provide enough MW power (without spurious heating) and apply strong enough and precisely oriented bias magnetic fields. Therefore, an integrated solution in the form of a chip-scale cryo-compatible device, with footprint below a few square millimeters, and which embeds a d.c. supplied MW oscillator and antenna, would be a valuable commodity for ODMR experiments. Such devices have already been developed in the context of conventional electron and nuclear spin resonance spectroscopy[141].

Regarding MW generation, voltage-controlled oscillators (VCOs) are inexpensive and compact alternatives to high-end MW sources, and lowering their phase noise would make them more useful for advanced measurements. Design of MW antennas delivering strong and homogeneous driving fields over wide areas is still in progress.

For single-emitter ODMR, both the digital single photon counting modules and the time tagging electronics drive the costs of the setup higher (typically 5'000 EUR each). As a cheaper alternative to the latter, FPGAs can be programmed for photon counting to yield much better temporal resolution than an NI card. An open-source package based on a commonly available FPGA for a do-it-yourself time tagger would make single emitter measurements more accessible.

For generating complex, long and low noise pulse sequences, NI cards reach their limits. As above, FPGA-based open-source solutions have the potential to make such experiments accessible at lower costs and with a high degree of customization for specific needs.

ACKNOWLEDGMENTS

This project has received funding from the Swiss National Science Foundation (grants No. PZ00P2_185824 and PP00P2_170684), from the European Union's Horizon 2020 research and innovation programme under the Marie Skł odowska-Curie grant agreement No 754354, and from EPFL Interdisciplinary Seed Fund.

AUTHOR DECLARATIONS

Conflict of Interest

The authors declare no conflicts of interest.

Author Contributions

H.S and H.B. contributed equally to this work. All authors wrote and discussed the manuscript.

DATA AVAILABILITY

The original and updated version of qudi are available on github[126,127].

[1]H. C. Ohanian, "What is spin?" American Journal of Physics **54**, 500 (1998).

[2]J. P. Dowling and G. J. Milburn, "Quantum technology: the second quantum revolution," Philosophical Transactions of the Royal Society of London. Series A: Mathematical, Physical and Engineering Sciences **361**, 1655–1674 (2003).

[3]L. M. K. Vandersypen, H. Bluhm, J. S. Clarke, A. S. Dzurak, R. Ishihara, A. Morello, D. J. Reilly, L. R. Schreiber, and M. Veldhorst, "Interfacing spin qubits in quantum dots and donors-hot, dense, and coherent," npj Quantum Information **3**, 1–10 (2017).

[4]X. Zhang, , H.-O. Li, , K. Wang, , G. Cao, , M. Xiao, , and G.-P. Guo, "Qubits based on semiconductor quantum dots*," Chinese Physics B **27**, 020305 (2018).

[5]H.-C. Chang, W. W.-W. Hsiao, and M.-C. Su, "Color Centers in Diamond," Fluorescent Nanodiamonds , 37–54 (2018).

[6]S. Castelletto and A. Boretti, "Silicon carbide color centers for quantum applications," Journal of Physics: Photonics **2**, 022001 (2020).

[7]S. Bertaina, S. Gambarelli, A. Tkachuk, I. N. Kurkin, B. Malkin, A. Stepanov, and B. Barbara, "Rare-earth solid-state qubits," Nature Nanotechnology **2**, 39–42 (2007).

[8]L. C. Camenzind, L. Yu, P. Stano, J. D. Zimmerman, A. C. Gossard, D. Loss, and D. M. Zumbühl, "Hyperfine-phonon spin relaxation in a single-electron GaAs quantum dot," Nature Communications **9**, 1–6 (2018).

[9]C. L. Degen, F. Reinhard, and P. Cappellaro, "Quantum sensing," Reviews of modern physics **89**, 035002 (2017).

[10]J. H. Wesenberg, A. Ardavan, G. A. D. Briggs, J. J. Morton, R. J. Schoelkopf, D. I. Schuster, and K. Mølmer, "Quantum computing with an electron spin ensemble," Physical Review Letters **103**, 070502 (2009).

[11]S. Pezzagna and J. Meijer, "Quantum computer based on color centers in diamond," Applied Physics Reviews **8**, 011308 (2021).

[12]R. Lescanne, S. Deléglise, E. Albertinale, U. Réglade, T. Capelle, E. Ivanov, T. Jacqmin, Z. Leghtas, and E. Flurin, "Irreversible Qubit-Photon Coupling for the Detection of Itinerant Microwave Photons," Physical Review X **10**, 021038 (2020).

[13]F. Dolde, V. Bergholm, Y. Wang, I. Jakobi, B. Naydenov, S. Pezzagna, J. Meijer, F. Jelezko, P. Neumann, T. Schulte-Herbrüggen, J. Biamonte, and J. Wrachtrup, "High-fidelity spin entanglement using optimal control," Nature Communications **5**, 1–9 (2014).

[14]A. Blank, E. Suhovoy, R. Halevy, L. Shtirberg, and W. Harneit, "ESR imaging in solid phase down to sub-micron resolution: methodology and applications," Physical Chemistry Chemical Physics **11**, 6689–6699 (2009).

[15]D. Suter, "Optical detection of magnetic resonance," Magnetic Resonance **1**, 115–139 (2020).

[16]J. Gugler, T. Astner, A. Angerer, J. Schmiedmayer, J. Majer, and P. Mohn, "Ab initio calculation of the spin lattice relaxation time T_1 for nitrogen-vacancy centers in diamond," PHYSICAL REVIEW B **98**, 214442 (2018).

[17]G. Balasubramanian, P. Neumann, D. Twitchen, M. Markham, R. Kolesov, N. Mizuochi, J. Isoya, J. Achard, J. Beck, J. Tissler, V. Jacques, P. R. Hemmer, F. Jelezko, and J. Wrachtrup, "Ultralong spin coherence time in isotopically engineered diamond." Nature materials **8**, 383–387 (2009).

[18]K. Nishimura, H. Kouno, Y. Kawashima, K. Orihashi, S. Fujiwara, K. Tateishi, T. Uesaka, N. Kimizuka, and N. Yanai, "Materials chemistry of triplet dynamic nuclear polarization," Chem. Commun. **56**, 7217–7232 (2020).

[19]J. M. Binder, A. Stark, N. Tomek, J. Scheuer, F. Frank, K. D. Jahnke, C. Müller, S. Schmitt, M. H. Metsch, T. Unden, T. Gehring, A. Huck, U. L. Andersen, L. J. Rogers, and F. Jelezko, "Qudi: A modular python suite for experiment control and data processing," SoftwareX **6**, 85–90 (2017).

[20]E. Bourgeois, M. Gulka, and M. Nesladek, "Photoelectric Detection and Quantum Readout of Nitrogen-Vacancy Center Spin States in Diamond," (2020).

[21]T. J. Penfold, E. Gindensperger, C. Daniel, and C. M. Marian, "Spin-Vibronic Mechanism for Intersystem Crossing," *Chemical Reviews*, **118** (2018), 10.1021/acs.chemrev.7b00617.

[22]C. M. Marian, "Spin-orbit coupling and intersystem crossing in molecules," Wiley Interdisciplinary Reviews: Computational Molecular Science **2**, 187–203 (2012).

[23]D. Carbonera, "Optically detected magnetic resonance (odmr) of photoexcited triplet states," Photosynthesis research **102**, 403–414 (2009).

[24]Kwiram, Alvin L., "Optical detection of paramagnetic resonance in phosphorescent triplet states," Chemical Physics Letters **1**, 272–275 (1967).

[25]J. Schmidt, I. A. Hesselmann, M. S. De Groot, and J. H. Van der Waals, "Optical detection of electron resonance transitions in phosphorescent quinoxaline," Chemical Physics Letters **1** (1967), 10.1016/0009-2614(67)85066-8.

[26]M. Sharnoff, "ESR-Produced Modulation of Triplet Phosphorescence," The Journal of Chemical Physics **46**, 3263 (2004).

[27]G. Giacometti, G. Agostini, S. Santabarbara, and D. Carbonera, "Odmr spectroscopy of molecular functions in photosynthetic membrane proteins," Applied Magnetic Resonance **31**, 179–191 (2007).

[28]A. Kwiram and J. Ross, "Optical detection of magnetic resonance in biologically important molecules," Annual Review of Biophysics and Bioengineering **11**, 223–249 (1982).

[29]J. Wrachtrup, C. v. Borczyskowski, J. Bernard, M. Orrit, and R. Brown, "Optically detected spin coherence of single molecules," Physical Review Letters **71**, 3565 (1993).

[30]J. Köhler, J. A. J. M. Disselhorst, M. C. J. M. Donckers, E. J. J. Groenen, J. Schmidt, and W. E. Moerner, "Magnetic resonance of a single molecular spin," Nature 1993 363:6426 **363**, 242–244 (1993).

[31]D. M. Arroo, N. M. N. Alford, and J. D. Breeze, "Perspective on room-temperature solid-state masers," Applied Physics Letters **119**, 140502 (2021).

[32]M. Oxborrow, J. D. Breeze, and N. M. Alford, "Room-temperature solid-state maser," Nature 2012 488:7411 **488**, 353–356 (2012).

[33]H. Wu, S. Mirkhanov, W. Ng, and M. Oxborrow, "Bench-Top Cooling of a Microwave Mode Using an Optically Pumped Spin Refrigerator," Physical Review Letters **127**, 053604 (2021).

[34]A. Gruber, A. Dräbenstedt, C. Tietz, L. Fleury, J. Wrachtrup, and C. V. Borczyskowski, "Scanning Confocal Optical Microscopy and Magnetic Resonance on Single Defect Centers," Science **276**, 2012–2014 (1997).

[35]G. Q. Liu, X. Feng, N. Wang, Q. Li, and R. B. Liu, "Coherent quantum control of nitrogen-vacancy center spins near 1000 kelvin," Nature Communications 2019 10:1 **10**, 1–8 (2019).

[36]M. Chipaux, K. J. v. d. Laan, S. R. Hemelaar, M. Hasani, T. Zheng, and R. Schirhagl, "Nanodiamonds and Their Applications in Cells," Small **14**, 1704263 (2018).

[37]S. Haziza, N. Mohan, Y. Loe-Mie, A. M. Lepagnol-Bestel, S. Massou, M. P. Adam, X. L. Le, J. Viard, C. Plancon, R. Daudin, P. Koebel, E. Dorard, C. Rose, F. J. Hsieh, C. C. Wu, B. Potier, Y. Herault, C. Sala, A. Corvin, B. Allinquant, H. C. Chang, F. Treussart, and M. Simonneau, "Fluorescent nanodiamond tracking reveals intraneuronal transport abnormalities induced by brain-disease-related genetic risk factors," Nature Nanotechnology **12** (2017), 10.1038/nnano.2016.260.

[38]S. Hemelaar, P. De Boer, M. Chipaux, W. Zuidema, T. Hamoh, F. P. Martinez, A. Nagl, J. Hoogenboom, B. Giepmans, and R. Schirhagl, "Nanodiamonds as multi-purpose labels for microscopy," Scientific reports **7**, 1–9 (2017).

[39]B. S. Miller, L. Bezinge, H. D. Gliddon, D. Huang, G. Dold, E. R. Gray, J. Heaney, P. J. Dobson, E. Nastouli, J. J. Morton, *et al.*, "Spin-enhanced nanodiamond biosensing for ultrasensitive diagnostics," Nature **587**, 588–593 (2020).

[40]A. Morita, A. C. Nusantara, F. P. P. Martinez, T. Hamoh, V. G. Damle, K. J. van der Laan, A. Sigaeva, T. Vedelaar, M. Chang, M. Chipaux, and R. Schirhagl, "Quantum monitoring the metabolism of individual yeast mutant strain cells when aged, stressed or treated with antioxidant," (2020).

[41]T. Zhang, G. Pramanik, K. Zhang, M. Gulka, L. Wang, J. Jing, F. Xu, Z. Li, Q. Wei, P. Cigler, *et al.*, "Toward quantitative bio-sensing with nitrogen–vacancy center in diamond," ACS sensors **6**, 2077–2107 (2021).

[42]J. F. Barry, J. M. Schloss, E. Bauch, M. J. Turner, C. A. Hart, L. M. Pham, and R. L. Walsworth, "Sensitivity optimization for NV-diamond magnetometry," Reviews of Modern Physics **92**, 15004 (2020).

[43]R. Schirhagl, K. Chang, M. Loretz, and C. L. Degen, "Nitrogen-vacancy centers in diamond: nanoscale sensors for physics and biology," Annual review of physical chemistry **65**, 83–105 (2014).

[44]L. Rondin, J.-P. Tetienne, T. Hingant, J.-F. Roch, P. Maletinsky, and V. Jacques, "Magnetometry with nitrogen-vacancy defects in diamond," Reports on progress in physics **77**, 056503 (2014).

[45]L. Shao, R. Liu, M. Zhang, A. V. Shneidman, X. Audier, M. Markham, H. Dhillon, D. J. Twitchen, Y.-F. Xiao, and M. Lončar, "Wide-Field Optical Microscopy of Microwave Fields Using Nitrogen-Vacancy Centers in Diamonds," Advanced Optical Materials (2016), 10.1002/adom.201600039.

[46]M. Chipaux, L. Toraille, C. Larat, L. Morvan, S. Pezzagna, J. Meijer, and T. Debuisschert, "Wide bandwidth instantaneous radio frequency spectrum analyzer based on nitrogen vacancy centers in diamond," Applied Physics Letters **107**, 233502 (2015).

[47]J. Meinel, V. Vorobyov, B. Yavkin, D. Dasari, H. Sumiya, S. Onoda, J. Isoya, and J. Wrachtrup, "Heterodyne sensing of microwaves with a quantum sensor," Nature Communications 2021 12:1 **12**, 1–8 (2021).

[48]A. J. Healey, L. T. Hall, G. A. L. White, T. Teraji, M.-A. Sani, F. Separovic, J.-P. Tetienne, and L. C. L. Hollenberg, "Polarization Transfer to External Nuclear Spins Using Ensembles of Nitrogen-Vacancy Centers," Physical Review Applied **10**, 54052 (2021).

[49]R. Rizzato, F. Bruckmaier, K. S. Liu, S. J. Glaser, and D. B. Bucher, "Polarization Transfer from Optically Pumped Ensembles of N-V Centers to Multinuclear Spin Baths," PHYSICAL REVIEW APPLIED **17**, 24067 (2022).

[50]X. Gao, S. Vaidya, K. Li, P. Ju, B. Jiang, Z. Xu, A. E. L. Allcca, K. Shen, T. Taniguchi, K. Watanabe, *et al.*, "Nuclear spin polarization and control in a van der waals material," arXiv preprint arXiv:2203.13184 (2022).

[51]H. J. Mamin, M. H. Sherwood, and D. Rugar, "Detecting external electron spins using nitrogen-vacancy centers," Physical Review B - Condensed Matter and Materials Physics **86**, 1–8 (2012).

[52]T. Staudacher, F. Shi, S. Pezzagna, J. Meijer, J. Du, C. a. Meriles, F. Reinhard, and J. Wrachtrup, "Nuclear magnetic resonance spectroscopy on a (5-nanometer)3 sample volume." Science (New York, N.Y.) **339**, 561–3 (2013).

[53]A. O. Sushkov, I. Lovchinsky, N. Chisholm, R. L. Walsworth, H. Park, and M. D. Lukin, "Magnetic resonance detection of individual proton spins using quantum reporters," Physical Review Letters **113** (2014), 10.1103/PhysRevLett.113.197601.

[54]I. Lovchinsky, A. O. Sushkov, E. Urbach, N. P. De Leon, S. Choi, K. De Greve, R. Evans, R. Gertner, E. Bersin, C. Muller, L. McGuinness, F. Jelezko, R. L. Walsworth, H. Park, and M. D. Lukin, "Nuclear magnetic resonance detection and spectroscopy of single proteins using quantum logic," Science **351**, 836–841 (2016).

[55]C. E. Bradley, J. Randall, M. H. Abobeih, R. C. Berrevoets, M. J. Degen, M. A. Bakker, M. Markham, D. J. Twitchen, and T. H. Taminiau, "A Ten-Qubit Solid-State Spin Register with Quantum Memory up to One Minute," Physical Review X **9**, 031045 (2019).

[56]B. Hensen, H. Bernien, A. E. Dréau, A. Reiserer, N. Kalb, M. S. Blok, J. Ruitenberg, R. F. Vermeulen, R. N. Schouten, C. Abellán, W. Amaya, V. Pruneri, M. W. Mitchell, M. Markham, D. J. Twitchen, D. Elkouss, S. Wehner, T. H. Taminiau, and R. Hanson, "Loophole-free Bell inequality violation using electron spins separated by 1.3 kilometres," Nature **526**, 682–686 (2015).

[57]C. Bradac, W. Gao, J. Forneris, M. E. Trusheim, and I. Aharonovich, "Quantum nanophotonics with group iv defects in diamond," Nature Communications **10**, 1–13 (2019).

[58]B. Pingault, D. D. Jarausch, C. Hepp, L. Klintberg, J. N. Becker, M. Markham, C. Becher, and M. Atatüre, "Coherent control of the silicon-vacancy spin in diamond," Nature Communications **8** (2017), 10.1038/ncomms15579.

[59]Z.-H. Zhang, P. Stevenson, G. Thiering, B. C. Rose, D. Huang, A. M. Edmonds, M. L. Markham, S. A. Lyon, A. Gali, and N. P. De Leon, "Optically Detected Magnetic Resonance in Neutral Silicon Vacancy Centers in Diamond via Bound Exciton States," PHYSICAL REVIEW LETTERS **125**, 237402 (2020).

[60]P. Siyushev, M. H. Metsch, A. Ijaz, J. M. Binder, M. K. Bhaskar, D. D. Sukachev, A. Sipahigil, R. E. Evans, C. T. Nguyen, M. D. Lukin, P. R. Hemmer, Y. N. Palyanov, I. N. Kupriyanov, Y. M. Borzdov, L. J. Rogers, and F. Jelezko, "Optical and microwave control of germanium-vacancy center spins in diamond," Physical Review B **96**, 081201 (2017).

[61]T. Iwasaki, Y. Miyamoto, T. Taniguchi, P. Siyushev, M. H. Metsch, F. Jelezko, and M. Hatano, "Tin-Vacancy Quantum Emitters in Diamond," Physical Review Letters **119** (2017), 10.1103/PhysRevLett.119.253601.

[62]R. Nagy, M. Widmann, M. Niethammer, D. B. Dasari, I. Gerhardt, Ã. O. Soykal, M. Radulaski, T. Ohshima, J. Vučković, N. T. Son, I. G. Ivanov, S. E. Economou, C. Bonato, S. Y. Lee, and J. Wrachtrup, "Quantum Properties of Dichroic Silicon Vacancies in Silicon Carbide," Physical Review Applied **9** (2018), 10.1103/PhysRevApplied.9.034022.

[63]F.-F. Yan, A.-L. Yi, J.-F. Wang, Q. Li, P. Yu, J.-X. Zhang, A. Gali, Y. Wang, J.-S. Xu, X. Ou, C.-F. Li, and G.-C. Guo, "Room-temperature coherent control of implanted defect spins in silicon carbide," npj Quantum Information 2020 6:1 **6**, 1–6 (2020).

[64]H. L. Stern, Q. Gu, J. Jarman, S. Eizagirre Barker, N. Mendelson, D. Chugh, S. Schott, H. H. Tan, H. Sirringhaus, I. Aharonovich, and M. Atatüre, "Room-temperature optically detected magnetic resonance of single defects in hexagonal boron nitride," Nature Communications 2022 13:1 **13**, 1–9 (2022).

[65]F. F. Murzakhanov, G. V. Mamin, S. B. Orlinskii, U. Gerstmann, W. G. Schmidt, T. Biktagirov, I. Aharonovich, A. Gottscholl, A. Sperlich, V. Dyakonov, and V. A. Soltamov, "Electron-nuclear coherent coupling and nuclear spin readout through optically polarized vb-spin states in hbn," Nano Letters **22**, 2718–2724 (2022), pMID: 35357842, https://doi.org/10.1021/acs.nanolett.1c04610.

[66]T. Zhong and P. Goldner, "Emerging rare-earth doped material platforms for quantum nanophotonics," Nanophotonics **8**, 2003–2015 (2019).

[67]M. Grimm, A. Beckert, G. Aeppli, and M. Müller, "Universal quantum computing using electronuclear wavefunctions of rare-earth ions," PRX Quantum **2**, 010312 (2021).

[68]K. Xia, R. Kolesov, Y. Wang, P. Siyushev, R. Reuter, T. Kornher, N. Kukharchyk, A. D. Wieck, B. Villa, S. Yang, *et al.*, "All-optical preparation of coherent dark states of a single rare earth ion spin in a crystal," Physical review letters **115**, 093602 (2015).

[69]X. Zhou, H. Liu, Z. He, B. Chen, and J. Wu, "Investigation of the electronic structure and optical, epr, and odmr spectroscopic properties for 171yb3+-doped y2sio5crystal: A combined theoretical approach," Inorganic Chemistry **59** (2020), 10.1021/acs.inorgchem.0c01430.

[70]A. Ortu, A. Holzäpfel, J. Etesse, and M. Afzelius, "Storage of photonic time-bin qubits for up to 20 ms in a rare-earth doped crystal," npj Quantum Information **8**, 1–7 (2022).

[71]V. Y. Ivanov, T. S. Shamirzaev, D. R. Yakovlev, A. K. Gutakovskii, L. Owczarczyk, and M. Bayer, "Optically detected magnetic resonance of photoexcited electrons in (In,Al)As/AlAs quantum dots with indirect band gap and type-I band alignment," PHYSICAL REVIEW B **97**, 245306 (2018).

[72]D. O. Tolmachev, V. Yu. Ivanov, D. R. Yakovlev, E. V. Shornikova, Bartłomiej Witkowski, Sushant Shendre, Furkan Isik, Savas Delikani, H. Volkan Demir, and Manfred Bayer, "Optically detected magnetic resonance in CdSe/CdMnS nanoplatelets," Nanoscale **12**, 21932–21939 (2020).

[73]A. Agostini, L. Nicol, N. Da Roit, M. Bortolus, R. Croce, and D. Carbonera, "Altering the exciton landscape by removal of specific chlorophylls in monomeric LHCII provides information on the sites of triplet formation and quenching by means of ODMR and EPR spectroscopies," Biochimica et Biophysica Acta (BBA) - Bioenergetics **1862**, 148481 (2021).

[74]J. N. Becker and E. Neu, "Chapter seven - the silicon vacancy center in diamond," in *Diamond for Quantum Applications Part 1*, Semiconductors and Semimetals, Vol. 103, edited by C. E. Nebel, I. Aharonovich, N. Mizuochi, and M. Hatano (Elsevier, 2020) pp. 201–235.

[75]D. Chen, N. Zheludev, and W.-b. Gao, "Building blocks for quantum network based on group-iv split-vacancy centers in diamond," Advanced Quantum Technologies **3**, 1900069 (2020).

[76]a. Dréau, M. Lesik, L. Rondin, P. Spinicelli, O. Arcizet, J.-F. F. Roch, and V. Jacques, "Avoiding power broadening in optically detected magnetic resonance of single NV defects for enhanced dc magnetic field sensitivity," Physical Review B - Condensed Matter and Materials Physics **84**, 195204 (2011).

[77]L. M. Vandersypen and I. L. Chuang, "Nmr techniques for quantum control and computation," Reviews of modern physics **76**, 1037 (2005).

[78]J.-P. Tetienne, T. Hingant, L. Rondin, A. Cavaillès, L. Mayer, G. Dantelle, T. Gacoin, J. Wrachtrup, J.-F. Roch, and V. Jacques, "Spin relaxometry of single nitrogen-vacancy defects in diamond nanocrystals for magnetic noise sensing," Physical Review B **87**, 235436 (2013).

[79] M. Rollo, A. Finco, R. Tanos, F. Fabre, T. Devolder, I. Robert-Philip, and V. Jacques, "Quantitative study of the response of a single nv defect in diamond to magnetic noise," Physical Review B **103**, 235418 (2021).

[80] J. Barton, M. Gulka, J. Tarabek, Y. Mindarava, Z. Wang, J. Schimer, H. Raabova, J. Bednar, M. B. Plenio, F. Jelezko, M. Nesladek, and P. Cigler, "Nanoscale Dynamic Readout of a Chemical Redox Process Using Radicals Coupled with Nitrogen-Vacancy Centers in Nanodiamonds," ACS Nano (2020), 10.1021/acsnano.0c04010.

[81] M. Chipaux, A. Tallaire, J. Achard, S. Pezzagna, J. Meijer, V. Jacques, J.-F. Roch, and T. Debuisschert, "Magnetic imaging with an ensemble of nitrogen-vacancy centers in diamond," Eur. Phys. J. D **69** (2015), 10.1140/epjd/e2015-60080-1.

[82] T. Wolf, P. Neumann, K. Nakamura, H. Sumiya, T. Ohshima, J. Isoya, and J. Wrachtrup, "Subpicotesla diamond magnetometry," Physical Review X **5**, 041001 (2015).

[83] H. Clevenson, M. E. Trusheim, C. Teale, T. Schröder, D. Braje, and D. Englund, "Broadband magnetometry and temperature sensing with a light-trapping diamond waveguide," Nature Physics **11**, 393–397 (2015).

[84] J. L. Webb, L. Troise, N. W. Hansen, C. Olsson, A. M. Wojciechowski, J. Achard, O. Brinza, R. Staacke, M. Kieschnick, J. Meijer, *et al.*, "Detection of biological signals from a live mammalian muscle using an early stage diamond quantum sensor," Scientific reports **11**, 1–11 (2021).

[85] J. Jonkman, C. M. Brown, G. D. Wright, K. I. Anderson, and A. J. North, "Tutorial: guidance for quantitative confocal microscopy," *Nature Protocols*, **15** (2020), 10.1038/s41596-020-0313-9.

[86] E. V. Levine, M. J. Turner, P. Kehayias, C. A. Hart, N. Langellier, R. Trubko, D. R. Glenn, R. R. Fu, and R. L. Walsworth, "Principles and techniques of the quantum diamond microscope," Nanophotonics **8**, 1945–1973 (2019).

[87] S. Nomura, "Wide-field imaging using ensembles of nv centers in diamond," in *Hybrid Quantum Systems* (Springer, 2021) pp. 27–42.

[88] S. C. Scholten, A. J. Healey, I. O. Robertson, G. J. Abrahams, D. A. Broadway, and J. P. Tetienne, "Widefield quantum microscopy with nitrogen-vacancy centers in diamond: Strengths, limitations, and prospects," (2021).

[89] A. M. Wojciechowski, M. Karadas, A. Huck, C. Osterkamp, S. Jankuhn, J. Meijer, F. Jelezko, and U. L. Andersen, "Contributed review: Camera-limits for wide-field magnetic resonance imaging with a nitrogen-vacancy spin sensor," Review of Scientific Instruments **89**, 031501 (2018).

[90] A. Kuwahata, T. Kitaizumi, K. Saichi, T. Sato, R. Igarashi, T. Ohshima, Y. Masuyama, T. Iwasaki, M. Hatano, F. Jelezko, *et al.*, "Magnetometer with nitrogen-vacancy center in a bulk diamond for detecting magnetic nanoparticles in biomedical applications," Scientific reports **10**, 1–9 (2020).

[91] W. G. Jerome and R. L. Price, *Basic confocal microscopy* (Springer, 2018).

[92] W. W.-W. Hsiao, Y. Y. Hui, P.-C. Tsai, and H.-C. Chang, "Fluorescent nanodiamond: a versatile tool for long-term cell tracking, super-resolution imaging, and nanoscale temperature sensing," Accounts of chemical research **49**, 400–407 (2016).

[93] D. Jin, P. Xi, B. Wang, L. Zhang, J. Enderlein, and A. M. van Oijen, "Nanoparticles for super-resolution microscopy and single-molecule tracking," Nature methods **15**, 415–423 (2018).

[94] O. R. Opaluch, N. Oshnik, R. Nelz, and E. Neu, "Optimized planar microwave antenna for nitrogen vacancy center based sensing applications," Nanomaterials **11**, 2108 (2021).

[95] K. Sasaki, Y. Monnai, S. Saijo, R. Fujita, H. Watanabe, J. Ishi-Hayase, K. M. Itoh, and E. Abe, "Broadband, large-area microwave antenna for optically detected magnetic resonance of nitrogen-vacancy centers in diamond," Review of Scientific Instruments **87**, 053904 (2016).

[96] I. Aharonovich, S. Castelletto, D. Simpson, C.-H. Su, A. Greentree, and S. Prawer, "Diamond-based single-photon emitters," Reports on progress in Physics **74**, 076501 (2011).

[97] S. D. Tchernij, T. Herzig, J. Forneris, J. Kupper, S. Pezzagna, P. Traina, E. Moreva, I. Degiovanni, G. Brida, N. Skukan, *et al.*, "Single-photon-emitting optical centers in diamond fabricated upon sn implantation," ACS photonics **4**, 2580–2586 (2017).

[98] D. G. Monticone, K. Katamadze, P. Traina, E. Moreva, J. Forneris, I. Ruo-Berchera, P. Olivero, I. P. Degiovanni, G. Brida, and M. Genovese, "Beating the abbe diffraction limit in confocal microscopy via nonclassical photon statistics," Physical review letters **113**, 143602 (2014).

[99] E. Abe and K. Sasaki, "Tutorial: Magnetic resonance with nitrogen-vacancy centers in diamond-microwave engineering, materials science, and magnetometry," Journal of Applied Physics **123**, 161101 (2018).

[100] J. Herrmann, M. A. Appleton, K. Sasaki, Y. Monnai, T. Teraji, K. M. Itoh, and E. Abe, "Polarization-and frequency-tunable microwave circuit for selective excitation of nitrogen-vacancy spins in diamond," Applied Physics Letters **109**, 183111 (2016).

[101] K. Bayat, J. Choy, M. Farrokh Baroughi, S. Meesala, and M. Loncar, "Efficient, uniform, and large area microwave magnetic coupling to nv centers in diamond using double split-ring resonators," Nano letters **14**, 1208–1213 (2014).

[102] H. Zheng, J. Xu, G. Z. Iwata, T. Lenz, J. Michl, B. Yavkin, K. Nakamura, H. Sumiya, T. Ohshima, J. Isoya, J. Wrachtrup, A. Wickenbrock, and D. Budker, "Zero-Field Magnetometry Based on Nitrogen-Vacancy Ensembles in Diamond," **11**, 1 (2019).

[103] F. Dolde, H. Fedder, M. W. Doherty, T. Nöbauer, F. Rempp, G. Balasubramanian, T. Wolf, F. Reinhard, L. C. Hollenberg, F. Jelezko, *et al.*, "Electric-field sensing using single diamond spins," Nature Physics **7**, 459–463 (2011).

[104] J. Michl, J. Steiner, A. Denisenko, A. Bülau, A. Zimmermann, K. Nakamura, H. Sumiya, S. Onoda, P. Neumann, J. Isoya, *et al.*, "Robust and accurate electric field sensing with solid state spin ensembles," Nano letters **19**, 4904–4910 (2019).

[105] E. Moreva, E. Bernardi, P. Traina, A. Sosso, S. D. Tchernij, J. Forneris, F. Picollo, G. Brida, Ž. Pastuović, I. Degiovanni, *et al.*, "Practical applications of quantum sensing: A simple method to enhance the sensitivity of nitrogen-vacancy-based temperature sensors," Physical Review Applied **13**, 054057 (2020).

[106] H. Kraus, V. Soltamov, F. Fuchs, D. Simin, A. Sperlich, P. Baranov, G. Astakhov, and V. Dyakonov, "Magnetic field and temperature sensing with atomic-scale spin defects in silicon carbide," Scientific reports **4**, 1–8 (2014).

[107] V. Ivády, H. Zheng, A. Wickenbrock, L. Bougas, G. Chatzidrosos, K. Nakamura, H. Sumiya, T. Ohshima, J. Isoya, D. Budker, *et al.*, "Photoluminescence at the ground-state level anticrossing of the nitrogen-vacancy center in diamond: A comprehensive study," Physical Review B **103**, 035307 (2021).

[108] D. A. Broadway, J. D. Wood, L. T. Hall, A. Stacey, M. Markham, D. A. Simpson, J.-P. Tetienne, and L. C. Hollenberg, "Anticrossing spin dynamics of diamond nitrogen-vacancy centers and all-optical low-frequency magnetometry," Physical Review Applied **6**, 064001 (2016).

[109] R. Lazda, L. Busaite, A. Berzins, J. Smits, F. Gahbauer, M. Auzinsh, D. Budker, and R. Ferber, "Cross-relaxation studies with optically detected magnetic resonances in nitrogen-vacancy centers in diamond in external magnetic field," Physical Review B **103**, 134104 (2021).

[110] A. Wickenbrock, H. Zheng, L. Bougas, N. Leefer, S. Afach, A. Jarmola, V. M. Acosta, and D. Budker, "Microwave-free magnetometry with nitrogen-vacancy centers in diamond," Applied Physics Letters **109**, 053505 (2016).

[111] V. Jacques, P. Neumann, J. Beck, M. Markham, D. Twitchen, J. Meijer, F. Kaiser, G. Balasubramanian, F. Jelezko, and J. Wrachtrup, "Dynamic polarization of single nuclear spins by optical pumping of nitrogen-vacancy color centers in diamond at room temperature," Physical review letters **102**, 057403 (2009).

[112] E. Bauch, C. A. Hart, J. M. Schloss, M. J. Turner, J. F. Barry, P. Kehayias, S. Singh, and R. L. Walsworth, "Ultralong dephasing times in solid-state spin ensembles via quantum control," Physical Review X **8**, 031025 (2018).

[113] C. A. Hart, J. M. Schloss, M. J. Turner, P. J. Scheidegger, E. Bauch, and R. L. Walsworth, "N-v–diamond magnetic microscopy using a double quantum 4-ramsey protocol," Physical Review Applied **15**, 044020 (2021).

[114] J. Choi, "Quantum many-body dynamics of a disordered electronic spin ensemble in diamond," (2019).

[115] C. Zhang, H. Yuan, N. Zhang, L. Xu, J. Zhang, B. Li, and J. Fang, "Vector magnetometer based on synchronous manipulation of nitrogen-vacancy centers in all crystal directions," Journal of Physics D: Applied Physics **51**, 155102 (2018).

[116] M. Crosser, S. Scott, A. Clark, and P. Wilt, "On the magnetic field near the center of helmholtz coils," Review of Scientific Instruments **81**, 084701 (2010).

[117]B. Yang, T. Murooka, K. Mizuno, K. Kim, H. Kato, T. Makino, M. Ogura, S. Yamasaki, M. E. Schmidt, H. Mizuta, *et al.*, "Vector electrometry in a wide-gap-semiconductor device using a spin-ensemble quantum sensor," Physical Review Applied **14**, 044049 (2020).

[118]J. L. Webb, L. Troise, N. W. Hansen, J. Achard, O. Brinza, R. Staacke, M. Kieschnick, J. Meijer, J.-F. Perrier, K. Berg-Sørensen, *et al.*, "Optimization of a diamond nitrogen vacancy centre magnetometer for sensing of biological signals," Frontiers in Physics **8**, 430 (2020).

[119]F. M. Stürner, A. Brenneis, T. Buck, J. Kassel, R. Rölver, T. Fuchs, A. Savitsky, D. Suter, J. Grimmel, S. Hengesbach, *et al.*, "Integrated and portable magnetometer based on nitrogen-vacancy ensembles in diamond," Advanced Quantum Technologies **4**, 2000111 (2021).

[120]G. R. Mirams, C. J. Arthurs, M. O. Bernabeu, R. Bordas, J. Cooper, A. Corrias, Y. Davit, S.-J. Dunn, A. G. Fletcher, D. G. Harvey, *et al.*, "Chaste: an open source c++ library for computational physiology and biology," PLoS computational biology **9**, e1002970 (2013).

[121]D.-S. Cao, Q.-S. Xu, Q.-N. Hu, and Y.-Z. Liang, "Chemopy: freely available python package for computational biology and chemoinformatics," Bioinformatics **29**, 1092–1094 (2013).

[122]B. Chapman and J. Chang, "Biopython: Python tools for computational biology," ACM Sigbio Newsletter **20**, 15–19 (2000).

[123]L. Prechelt, "An empirical comparison of seven programming languages," Computer **33**, 23–29 (2000).

[124]R. Bitter, T. Mohiuddin, and M. Nawrocki, *LabVIEW: Advanced programming techniques* (Crc Press, 2006).

[125]M. H. Cahn and M. F. Russo, "Python and automated laboratory system control," JALA: Journal of the Association for Laboratory Automation **12**, 46–55 (2007).

[126]"Qudi original github," `https://github.com/Ulm-IQO/qudi`.

[127]"Qudi github for the new version," `https://github.com/QexSoftware/qudi`.

[128]L. P. McGuinness, Y. Yan, A. Stacey, D. A. Simpson, L. T. Hall, D. Maclaurin, S. Prawer, P. Mulvaney, J. Wrachtrup, F. Caruso, and others, "Quantum measurement and orientation tracking of fluorescent nanodiamonds inside living cells," Nature nanotechnology **6**, 358–363 (2011).

[129]A. Sigaeva, A. Hochstetter, S. Bouyim, M. Chipaux, M. Stejfova, P. Cigler, and R. Schirhagl, "Single-particle tracking and trajectory analysis of fluorescent nanodiamonds in cell-free environment and live cells," with Small (2022), 1.

[130]"Signals and slots in qt documentation," `https://doc.qt.io/qt-5/signalsandslots.html`.

[131]"Qudi installation," `https://ulm-iqo.github.io/qudi-generated-docs/html-docs/installation.html`.

[132]"Conda environments in conda documentation," `https://docs.conda.io/projects/conda/en/latest/user-guide/concepts/environments.html`.

[133]B. J. Maertz, A. P. Wijnheijmer, G. D. Fuchs, M. E. Nowakowski, and D. D. Awschalom, "Vector magnetic field microscopy using nitrogen vacancy centers in diamond," Applied Physics Letters **96**, 092504 (2010), https://doi.org/10.1063/1.3337096.

[134]T. Lenz, A. Wickenbrock, F. Jelezko, G. Balasubramanian, and D. Budker, "Magnetic sensing at zero field with a single nitrogen-vacancy center," Quantum Science and Technology **6**, 034006 (2021).

[135]N. Wang, C.-F. Liu, J.-W. Fan, X. Feng, W.-H. Leong, A. Finkler, A. Denisenko, J. Wrachtrup, Q. Li, and R.-B. Liu, "Zero-field magnetometry using hyperfine-biased nitrogen-vacancy centers near diamond surfaces," Phys. Rev. Research **4**, 013098 (2022).

[136]K. Jensen, V. Acosta, A. Jarmola, and D. Budker, "Light narrowing of magnetic resonances in ensembles of nitrogen-vacancy centers in diamond," Physical Review B **87**, 014115 (2013).

[137]L. Robledo, H. Bernien, T. Van Der Sar, and R. Hanson, "Spin dynamics in the optical cycle of single nitrogen-vacancy centres in diamond," New Journal of Physics **13**, 025013 (2011).

[138]N. Aslam, G. Waldherr, P. Neumann, F. Jelezko, and J. Wrachtrup, "Photo-induced ionization dynamics of the nitrogen vacancy defect in diamond investigated by single-shot charge state detection," New Journal of Physics **15**, 013064 (2013).

[139]R. Giri, F. Gorrini, C. Dorigoni, C. E. Avalos, M. Cazzanelli, S. Tambalo, and A. Bifone, "Coupled charge and spin dynamics in high-density ensembles of nitrogen-vacancy centers in diamond," Phys. Rev. B **98**, 045401 (2018).

[140]A. Jarmola, V. Acosta, K. Jensen, S. Chemerisov, and D. Budker, "Temperature-and magnetic-field-dependent longitudinal spin relaxation in nitrogen-vacancy ensembles in diamond," Physical review letters **108**, 197601 (2012).

[141]A. V. Matheoud, N. Sahin, and G. Boero, "A single chip electron spin resonance detector based on a single high electron mobility transistor," Journal of Magnetic Resonance **294**, 59–70 (2018).